ROCK PROPERTIES OF SILURIAN NIAGARAN REEF CARBONATES IN MICHIGAN AFTER CO_2 INJECTION

Undergraduate Research Thesis
Submitted in partial fulfillment of the requirements for graduation
with research distinction in Earth Sciences
In the undergraduate colleges of
The Ohio State University

By

Laura E. Keister
The Ohio State University
2018

Approved by

David Cole, Advisor

School of Earth Sciences

TABLE OF CONTENTS

ABSTRACT

Carbon capture utilization and storage (CCUS) technologies have been implemented to extract hydrocarbons from depleted oil and gas reservoirs in the northern Silurian Niagaran reef trend in the Michigan Basin. This project analyzed rock properties from trim and intact core samples from a well that experienced CO_2 injection, and the rock properties were correlated with depth and diagenesis. Three thin sections from different depths, made from trim samples, were imaged using both digital and polarizing light microscopes. Images were used to analyze fractures, porosity, and mineralogy across the slides. The same features were analyzed for the intact core using X-ray CT and micro X-ray CT scans. All samples were examined with scanning electron microscopy (SEM) and X-ray diffraction (XRD) for microtextural, microanalytical, and bulk mineralogical analysis. The samples did not show strong correlations between porosity and depth. As depth increased, the amount of organic matter tended to decrease, and the amount of salt tended to increase. Two of the trim samples and the intact core have areas of the matrix that are disrupted by complex fracture systems that connect small pore spaces. Along the fractures and in the pore spaces, there is evidence of second generation precipitates of salts and carbonates. This suggests that these samples have undergone complex diagenesis over time after lithification. Further research is needed to understand whether or not CO_2 had an impact on development of fractures, dissolution, and mineralization.

ACKNOWLEDGEMENTS

I would like to thank Dr. David Cole, Dr. Julie Sheets, and Dr. Sue Welch for their outstanding advising and support through my undergraduate research experience. My research required a lot of training on lab equipment, analyses, and geochemistry that I was previously unfamiliar with, so their guidance and patience made this process smooth and fulfilling. This project was funded by the Department of Energy and made possible by the Battelle Memorial Institute Energy Group and The Ohio State University Subsurface Energy Materials Characterization and Analysis Laboratory (SEMCAL). Access to oil fields was made possible by Core Energy. Rock samples were provided by Battelle Memorial, and analysis was made possible by resources provided by SEMCAL. Thank you to all employees at Battelle involved in the Midwest Regional Carbon Sequestration Partnership who have enriched this experience by allowing me to continue involvement on the project at my internship. Dr. Dustin Crandall of National Energy and Technology Laboratory provided the micro XCT imagery, and Emma Oti and Dr. Ann Cook of the School of Earth Sciences, Ohio State University provided the macro XCT imagery. I would also like to thank Dr. Anne Carey and The Ohio State School of Earth Sciences for giving me guidance during my thesis writing process and allowing me to participate in such extensive research as an undergraduate. Also, thank you to Mr. and Mrs. Morgan and The School of Earth Sciences Field Experience Travel Fund for assisting me in funding my field experience in Utah. Finally, a personal thank you to my friends and family for their livelihood throughout my undergraduate career. I could not have done this without your love and support.

LIST OF FIGURES

LIST OF TABLES

INTRODUCTION

Carbon dioxide capture and storage (CCS) is an emerging global technology that allows for both the continued use of fossil fuels and the reduction of greenhouse gas (GHG) emissions (Carbon Sequestration Atlas of the United States and Canada, 2015). Commercial vendors and coal and gas-fired power plants are incorporating systems and technologies into their businesses to capture CO_2 that would otherwise be emitted into the atmosphere. Emissions from stationary facilities such as power plants, cement production, and fossil fuel refineries are responsible for 60% of GHG emissions (Oelkers and Cole, 2008). Ancillary systems convert the CO_2 into a supercritical form ($scCO_2$) that can be transported by pipelines to injection sites (Dooley et al., 2006). At these injection sites, the $scCO_2$ is injected deep into subsurface porous formations below low permeability caprock geologic formations. Today, most $scCO_2$ is injected into depleted oil and gas reservoirs because of their high pore volume and connectivity (Benson and Cole, 2008), but saline aquifers, unmineable coal seams, and saline-filled basalt formations also offer viable storage sites (Benson and Cole, 2008). Oil and gas companies are using these technologies for carbon capture storage and utilization (CCUS), an application of CCS, in depleted oil and gas reservoirs to enhance recovery of remaining fossil fuels through enhanced oil recovery (EOR). EOR involves injecting CO_2 to sweep oil towards producing wells, increasing recovery by 15-25% (Carbon Sequestration Atlas of the United States and Canada, 2015). This process is illustrated in **Figure 1** with $scCO_2$ injected in the injection well and oil extracted from the producing well.

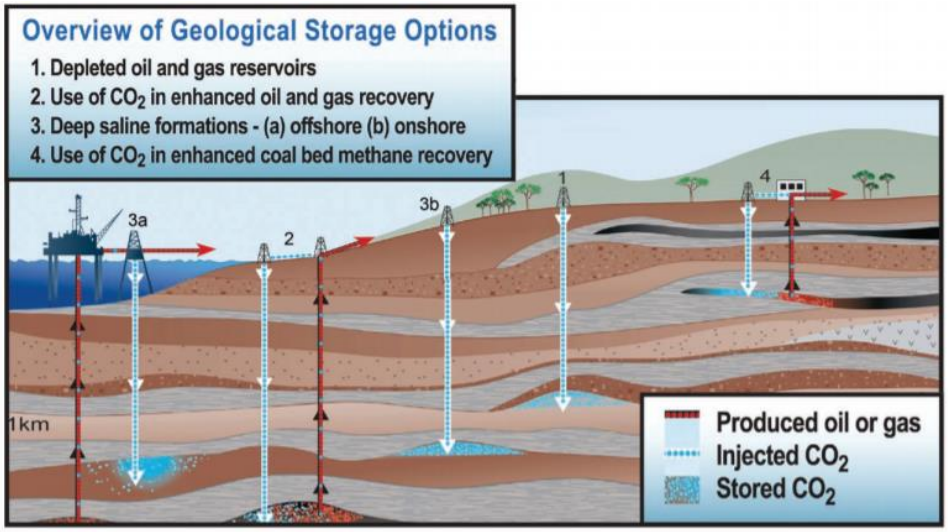

Figure 1. An illustration of injecting $scCO_2$ into different geologic formations. EOR is illustrated at 2, where the $scCO_2$ is injected and floods the reservoir, pushing the oil through to the producing well. This diagram was used from Benson and Cole, 2008 and originally modified from the Carbon Dioxide Cooperative Research Center (CO2CRC), http://www.co2crc.com.au/about/ co2crc.

Capture technologies also allow owners and operators to continue running their businesses while still meeting CO_2 emission restrictions. There are 26 gigatons (Gt) of CO_2 emitted annually, and a cumulative 9,000 gigatons could be emitted over the next century with increased standard of living

(Dooley et al., 2006). However, in 1992 the United Nations Framework Convention on Climate Change stated that emissions would have to be no more than 4,600 $GtCO_2$ to prevent "dangerous anthropogenic interference with the climate system." A billion metric tons needs to be sequestered annually to make a noticeable difference in GHGs, which is a 250 fold increase of current amounts (Benson and Cole, 2008). Oil and gas reservoirs alone are estimated to have a large enough capacity to store between 675 and 900 gigatons (Benson and Cole, 2008). Increasing the current scale of CCS projects would make reaching that goal much more realistic.

This method of climate change mitigation is environmentally friendly and cost effective (Dooley et al., 2006). Comprehensive site characterization is thoroughly conducted before injection can commence. Porous reservoirs overlain by impermeable seals are needed for storage, and there is extensive knowledge available about candidate sites around the world because of the oil and gas industry. Globally, there is an estimated potential for CCS projects to store 11,000 $GtCO_2$ in these sites at about $50 per ton (Dooley et al., 2006). Depleted oil and gas reservoirs are thousands of feet below freshwater sources, and their fluids have been trapped by caprocks for hundreds of millions of years. These low permeability caprocks are effective in trapping the buoyant, low density CO_2 (Oelkers and Cole, 2008). Also, fluid mobility is limited after injection due to high pressures allowing CO_2 to fill pores (Benson and Cole, 2008). Candidate sites are chosen in areas with negligible seismic activity and faulting. Therefore, the chance of leakage is very small. Extensive Monitoring, Verification and Accounting (MVA) systems, such as seismic imaging of fluids, wireline logging, remote sensing techniques, and pressure monitoring (Carbon Sequestration Atlas of the United States and Canada, 2015), are used to ensure safe and effective long-term storage.

Injected CO_2 can be trapped by stratigraphic and structural mechanisms, capillary pressures, solubility, and mineral trapping (Benson and Cole, 2008). The presence of stratigraphic and structural traps are determined pre-injection during site characterization. After injection, residual CO_2 can be immobilized and trapped in the pore spaces by water pressure (Benson and Cole, 2008). Over time, the CO_2 can dissolve into the pore water, making it less susceptible to buoyant forces (2008). On the scale of tens to thousands of years, mineral trapping can convert the CO_2 to stable carbon precipitates, but this depends on the presence of silicate minerals, saturation of the fluid, nucleation sites and rates, and the pores and minerals available for secondary mineralization (DePaolo and Cole, 2013). Although all of these mechanisms indicate that the CO_2 is remaining underground in the location it was injected (Carbon sequestration atlas of the United States and Canada, 2015), there is uncertainty regarding the extent to which these reactions can impact the strength and integrity of the rock (DePaolo and Cole, 2013). However, MVA is currently an area of intense research aiming to increase the understanding of the behavior of supercritical CO_2 and in deep formations. Continued development of accurate technologies and methods, adapted for each site, are necessary to detect possible slow, undetected leaks before they become an environmental danger. Long term research should be conducted on existing CCS sites to increase understanding of geophysical and geochemical risks, such as possible anthropogenic migration pathways caused by high injection pressures or chemical reactions degrading the rock integrity through dissolution. Ultimately, the ability to predict the fate of injected CO_2 and the reservoir rock can ensure that migration and degradation of rocks is not a major risk. Once there is a fundamental understanding of the behavior of CO_2 and assurance of public safety, more large-scale CCS projects can be implemented globally to significantly reduce GHG emissions.

The goal of this study was to contribute to MVA by conducting a rock property analysis of carbonate samples from a reef that experienced CO_2 injection, and to study the relationships between rock properties and reef location, diagenesis and depth in the reservoir. The samples were acquired from Michigan basin reefs where carbon sequestration and enhanced oil recovery projects have been occurring for decades. This study can provide a reference for those conducting future analysis on the effects of CO_2 on reservoir rocks. This would allow researchers to further study any changes in porosity, permeability, mineralogy, and fractures over time. It would be beneficial to conduct regular rock property analyses long term to mitigate any safety concerns regarding possible environmental risks.

GEOLOGIC SETTING

Reef Trends

Niagaran and lower Salina reef complexes formed throughout the Michigan Basin during the Silurian when they were situated less than 30°S of the equator (Friedman and Kopaska-Merkel, 1991). **Figure 2** shows the reef environments that formed on the basin-rimming ramp between a carbonate platform and the deep basin. These reefs are concentrated into two elongate, asymmetric, heterogeneous northern and southern belts. Each belt extends more than 100 miles long and 10-20 miles wide. Samples from this study originated from the ramp of the northern pinnacle reef belt in the Dover field, Otsego County, Michigan. This belt has a northeast to southwest trend and extends about 170 miles long and 15 miles wide (Gill, 1979). There are more than 700 pinnacle reef structures that have vuggy porosity and range in depth from 4,000 to 6,000 feet (Carbon sequestration atlas of the United States and Canada, 2015). The reefs are generally tens of acres in area, more than 500 feet high, and they dip 30 to 45 degrees towards the center of the basin where they thicken (Gill 1979). Stratigraphy of these reefs exhibits complex regional and local variations. The asymmetry was caused by the eastern paleowind direction which created narrow, steep slopes on the eastern margins and wider, gradual slopes with muddy and thin sediments on the west and southwest margins (Rine et al., 2017). Complex lateral and vertical variations over the shelf, ramp, and deep basin can also be attributed to changes in eustatic sea level and subsidence. Changes in sea level affected reef growth and salinity, caused varying depositional patterns, dolomitization, salt plugging (Sears and Lucia 1979), and resulted in alternating cycles of carbonate and evaporite formations (Friedman and Kopaska-Merkel, 1991). Thicker pinnacle reefs occur toward the basin due to the subsiding ramp and deeper water (Sears and Lucia, 1979). Basinward, the reefs become increasingly salt plugged, and degree of dolomitization and preserved secondary porosity increases toward the margins of the basin (Friedman and Kopaska-Merkel, 1991).

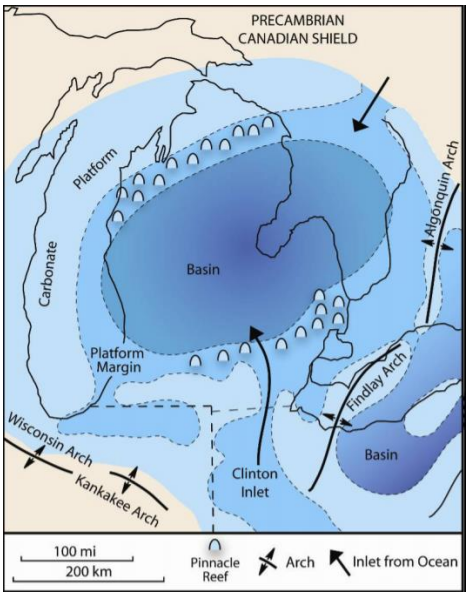

Figure 2. Silurian environments in Michigan with the two reef trends formed on along the north and south edges of the basin (figure from Grammer et al., 2010).

Hundreds of hydrocarbon-bearing reefs have been identified, while more than 50 have been determined to be salt plugged (Gill, 1979). The dolomitized cements are often associated with inclusions of organic material such as pyrobitumen (Cercone and Lohmann, 1987). These reefs and overlying units have been major targets for fossil fuel extraction and carbon sequestration due to their secondary porosity and organic content. Locations and depths of hydrocarbons change throughout the basin due to varying depositional conditions. **Figure 3** illustrates the northern belt from Manistee County to Otsego County and how hydrocarbon content varies over space. Towards the basin, fluid content transitions from water to oil to gas. This is controlled by increased burial depth and reservoir pressure towards the basin, and the fluids are partitioned based on dip direction and density (Gill, 1979).

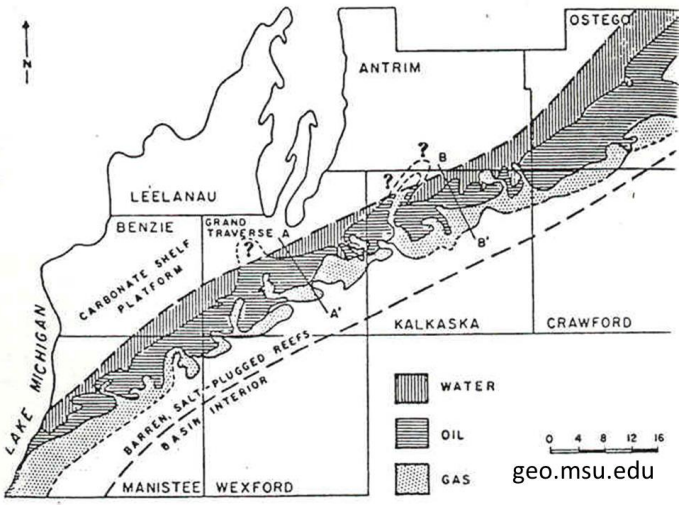

Figure 3. Map showing the northern reef trend in the Michigan Basin and where hydrocarbons are present. Samples supplied for this study are from an oil field in Otsego County. Here, the primary hydrocarbon is oil (figure from Schaetzl).

Reef Growth Models

There are many different models of reef growth that consider different hypotheses of sea level changes, basin subsidence, sediment depositional environments, and facies models. However, it is generally concluded that the Niagaran reefs grew in quiet, shallow marine water with frame building organisms followed by periods of rising and falling sea levels (Sears and Lucia, 1979). Dolomitization occurred during periods of subaerial exposure, which destroyed much of the primary reef fabric (Cercone and Lohmann, 1987) and increased porosity and permeability through leaching (Friedman and Kopaska-Merkel, 1991). This was due to both meteoric water and hypersaline brines that replaced the calcite with dolomite (Cercone and Lohmann, 1987). Changing sea levels influenced deposition of other lithologies in supra-tidal and tidal flat zones. These other lithologies are composed of evaporites, variations in limestones, some mudstone, and incorporations of stromatopods, algae, and many allochems. A current model of reef growth, developed by Rine in

2017 and shown in **Figure 4**, defines three stages of development and 11 major depositional environments: bioherm complex (the Niagaran unit), middle Niagaran reef complex, and the stromatolitic cap (uppermost Lower Salina A-1 Carbonate unit). The bioherm is divided into two depositional environments: the bioherm toe and the bioherm which were both below wave base in quiet water (Friedman and Kopaska-Merkel, 1991). The development of reef complex in stage 2 is divided into six depositional environments (windward distal foreslope, windward proximal foreslope, reef core, leeward proximal reef apron, leeward distal reef apron, and leeward toe-of-slope). These were identified by lateral variations in facies and extend from below wave base, to above, and ended below. In general, it is characterized by coral–stromatoporoid boundstone and skeletal wackestone facies with fossils of tabulate corals, stromatoporoids, and intrareef faunal assemblages of bryozoans, brachiopods, crinoids, and rugose corals. The stromatolitic cap is divided into windward distal foreslope, windward proximal foreslope, and tidal flat. This started below wave base and ended above (Rine et al., 2017). As shown below, the windward sides are steeper than the leeward sides and contain coarser sediments and better reservoir potential (Grammer et al., 2010). This created heterogeneity in facies stacking and reef geometry.

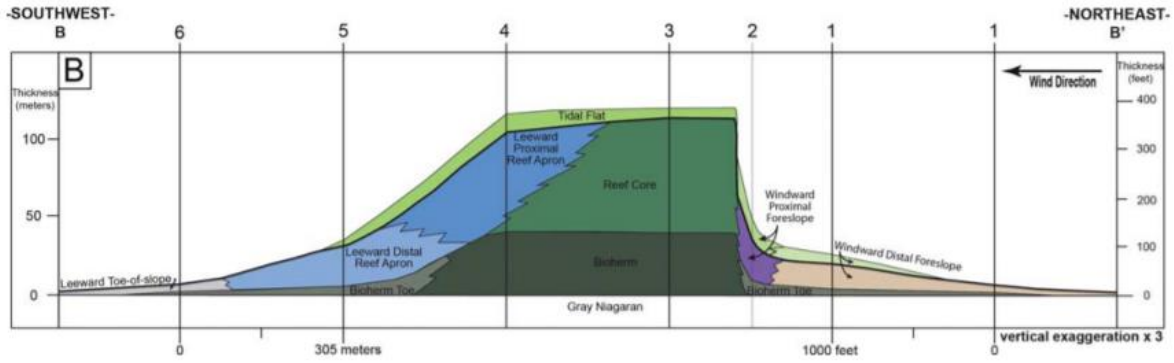

Figure 4. A three to one vertically exaggerated cross-section of Rine's reef model based on wind direction (Rine et al., 2017). Six adjacent wells were used to determine thickness. The bold black line divides Stage 2 from the stromatolitic cap. The eastern side has steeper slopes and coarser sediments, while the western side has gentler slopes and finer sediments due to paleowind direction.

Formations

During changes of sea level, basin subsidence, and environment conditions, alternating cycles of evaporites and carbonates were deposited. A simplified stratigraphic column is shown in **Figure 5**. Evaporite and carbonate deposition of the late Silurian pinnacle reefs are modeled having alternating periods of reef development and hyper salinity (Friedman and Kopaska-Merkel, 1991). The alternating sea level and hypersaline environments allowed carbonate, evaporite, and shale formations. As depth increases, the formations tend to become less salt rich and more carbonate rich (Caughlin et al., 1976). During periods of low sea level and subaerial exposure, formations were leached, and later plugged with vug-filling evaporites to varying degrees across the basin. Increases in salinity provided an impermeable layer above the reservoir (Friedman and Kopaska-Merkel, 1991). The reefs are underlain by low impermeability shale and limestone.

The reef core consists of the Niagaran unit which is made up of corals and stromatoporoid skeletons that were deposited in a shallow marine, low sediment supply environment (Gardner and Bray, 1984). This unit is made up of the Brown and Gray Niagaran, the A-0 carbonate, the A-1 evaporite, and the A-1 carbonate, which are the modern-day reservoir rocks. The source rocks are primarily the Niagaran and the Salina A-1 carbonates which are relatively thick, have a petroliferous odor, and show gas and oil (Gardner and Bray, 1984). The A-0 carbonate is made of dark mudstone deposited on the reef rubble adjacent to the reefs (Huh et al., 1977). The A-1 unit is made of a lower, thin anhydrite and evaporite unit and an upper carbonate unit of limestone in the basin center and dolomite on the margins (Sonnenfeld and Al-Aasm, 1991). During low stand the A-1 evaporites were deposited, followed by a rise in sea level and deposition of A-1 carbonates in a higher energy, wave-resistant environment (Caughlin et al., 1976). This unit was deposited during mesosaline conditions and surrounds the reefs as the stromatolitic cap (Huh et al., 1977). Evaporite precipitation filled much of the enhanced porosity caused by dolomitizaion, leading to some reefs being entirely salt plugged (Friedman and Kopaska-Merkel, 1991).

These rocks are overlain by the Silurian Salina Group, which are the modern-day seal rocks. Basin subsidence began during the start of their deposition at a rate of 0.5 mm per year (Sonnenfeld and Al-Aasm, 1991). In general, carbonate deposition is characteristic of slower subsidence (Sonnenfeld and Al-Aasm, 1991). The Silurian Salina Group exhibited five major cycles of evaporite and shale deposition for a duration of about 36,000 years. They are defined as A-2 evaporite, A-2 carbonate, B evaporite, C shale, D evaporite, E shale, F evaporite, and G shale. Some of the cycles cross each other, indicating rising sea level or subsidence. Increasing in depth towards the basin, the formations become less salt rich and more carbonate rich (Caughlin et al., 1976). Capping the oil and gas is the rapidly deposited, impermeable Salina A-2 evaporite that formed when sea level dropped, followed by the A-2 carbonate. The unit also seals the reefs that can be hundreds of feet tall and up to a mile in diameter (Gardner and Bray, 1984). The unit drapes over the reef and gets much thinner when transitioning to anhydrite on the rims of the deposition, which marks the transition from deep basin subsidence to moderate shelf subsidence (Sonnenfeld and Al-Aasm, 1991). Similar deposition cycles followed with the upper confining units above the reservoir (the A-2 carbonate through the G shale).

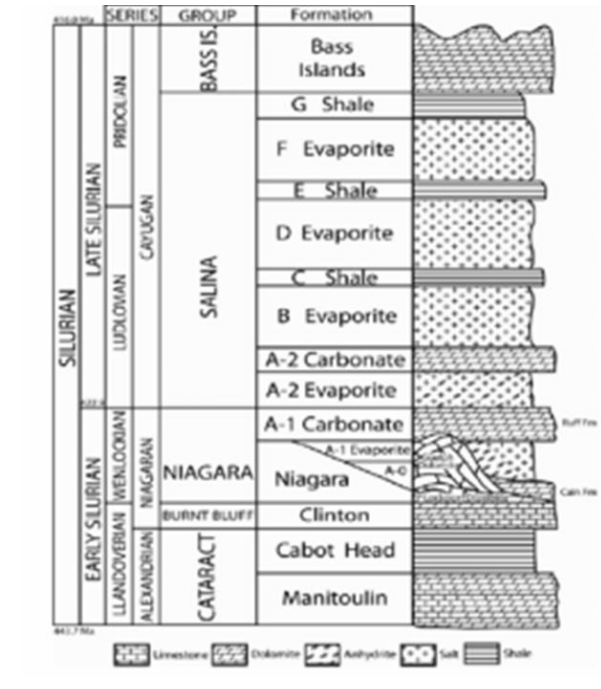

seisware.com

Figure 5. General stratigraphic column of the northern reef trend and confining units in the Michigan Basin. The Niagaran Group consists of the ancient reef material and is the modern-day reservoir. Capping this group is the Salina Group, consisting of many alternate layers of impermeable evaporites and shales (figure from Modroo et al., 2014).

Samples from this study were acquired from the reservoir rocks (The A-1 carbonate down to the Niagaran). Information was not provided for which samples originated from which formations and facies groups. However, the formations are associated with the reef core and tidal flat environments (Rine et al., 2017). Dolomitization and leaching made correlation with specific facies groups difficult.

METHODS

Sampling Methodology

The intact core samples and trimmed ends from sidewall cores from the Dover field in Otsego County, Michigan were provided by Battelle Memorial. The goal was to obtain 180 feet of core that encompassed the A-1 Carbonate down to the base of the Niagaran. The Subsurface Energy Materials Characterization and Analysis Laboratory (SEMCAL) at The Ohio State University was interested in studying cores above, near, and below the oil-water contact, so resistivity logs were used to estimate the interface depth at about 5627'-5639' with a transitional region from oil to water from 5643'-5685'. Three intact cores (1.5" diameter and 4" long) from depths 5606.1' (above oil-water interface), 5690.25' (below oil-water interface), and 5700' (above oil-water interface) and three trims from sidewall cores (1.5" diameter and 1/4" to 1/2" long) from depths 5588' (above oil-water interface), 5630' (within oil-water interface), and 5655' (transition zone) were then sent to Ohio State. Each sample and its position in the reservoir relative to the oil-water contact is displayed in **Table 1**. Thin and thick sections of the three samples were made by Spectrum Petrographics, Inc. (Vancouver, Washington).

Table 1. Samples, their depths, and their positions in the reservoir relative to the oil-water contact.

Sample	Depth	Location in the Reservoir
Trim 30	5588'	Above oil-water contact
Intact Core 5606.1'	5606.1'	Above oil-water contact
Trim 25	5630'	Within oil-water contact
Trim 20	5655'	Transitional region from oil to water
Intact Core 5690.25'	5690.25'	Below oil-water contact
Intact Core 5700'	5700'	Below oil-water contact

X-Ray Diffraction Analysis

A PANalytical X'Pert Pro X-ray diffractometer available at SEMCAL, School of Earth Sciences, OSU, was used for X-ray diffraction analysis to determine bulk mineralogy of the three trim samples and composition of vug material for the 5690' core (below oil-water interface). Corners were taken off the trim samples and ground by hand with an agate mortar and pestle. Vug-filling minerals from the core sample were picked out by hand after the intact core was broken with a rock hammer. These were medium silt to coarse sand sized (0.02 mm to 0.4 mm) grains (determined by SEM

images). For each sample, approximately one gram of material was loaded directly into standard sample holders. Samples were scanned with CuKα radiation from 4.0 to 70.0º 2-theta, 0.02º 2θ per step (count time 20 s per step) at 45 kV, 40 mA. PANalytical HighScore Plus, Data Viewer, and PDF 4+ database were used for qualitative mineralogical analysis and determination of bulk composition.

Imaging

To analyze rock properties, Dover thin section slides were photographed using both a Leica DMS 1000 digital light microscope and an Olympus SX50 polarizing light microscope. During this process, changes in birefringence, pore distribution, and presence of fractures were examined on the centimeter to millimeter scale. Thin section slides of trims 20, 25, and 30 were placed under both low and high magnification for the digital light microscope and under low magnification for the polarizing light microscope. All three slides were imaged by the digital light microscope camera by placing them in the field of view and acquiring images of the whole slide as well as magnified portions. All three slides were completely documented by the polarizing light microscope camera by positioning one corner in the field of view, acquiring the image, then gradually working down the side. This was repeated from the left to right side, and all neighboring acquired images contained overlap. Because the digital light microscope images were taken at a different orientation, the images were rotated throughout this project for orientation consistency. Blue dyed epoxy was used to impregnate the samples and stabilize them for grinding and polishing. Using the photomicrographs, areas of interest were later correlated with the slides' positions in the scanning electron microscope (SEM) for more detailed analysis.

Scanning Electron Microscopy and X-ray Computed Tomography

A FEI Quanta 250 Field Emission Gun Scanning Electron Microscope (SEM) in SEMCAL was used to study the composition of the matrix carbonate, identify accessory minerals, examine textures of pore spaces, and view fractures on the micrometer scale. Thin sections of all three depths and fragments of core from 5690' were studied.

Thin sections were coated with electrically conductive carbon material and adhered with copper tape to minimize charging buildup, and placed in the SEM. Images from the Leica digital light microscope and polarizing light microscope were correlated with the slides' positions in the SEM.

XCT scans of core 5690' displayed an area with contrasting densities attributed to differences in mineralogy within a vug. To identify the composition, the core needed to be broken into small enough pieces for X-ray diffraction analysis (XRD) and SEM evaluation. Rock fragments were collected by fracturing core samples near this zone of interest. Location on the core was determined by the XCT slice number and voxel resolution of each slice using imaging software programs. The rock core was wrapped in multiple layers of paper and cardboard for containment and struck with a hammer. Rock fragments were collected from the broken core and mounted on stubs with electrically conductive carbon tape using tweezers and gloves to avoid contamination. Stub A contained mineral crystals from the fractured area, stub B contained coarse grains from the fractured area, and stub C contained fine grains from the fractured area.

After placing thin sections and stubs in the SEM, energy-dispersive X-ray spectroscopy (EDXS) was used to identify chemical compositions at locations of interest. The characteristic X-ray peaks in the EDXS spectra aided in determining minerals present. All images were taken in backscattered mode.

For presentation purposes, brightness and contrast values were edited for dark images using Microsoft Word.

XCT Scans and Pixel Classification

Micro X-ray CT scans of the intact core from depth 5690' were produced by Dr. Dustin Crandall of National Energy Technology Laboratory (NETL) in Morgantown, WV. XCT scans of the intact core and trim from all six depths were produced by Emma Oti and Dr. Ann Cook of the School of Earth Sciences at Ohio State. The scans were provided as 2D stacked slices of the core that needed to be reconstructed for 3D view. Analysis of CT scans was started using core from depth 5690' based on interest in its hydrocarbon content. ImageJ (Fiji) and Avizo were used for rendering the 3D view by stacking the 2D image data. The image stack was loaded into ImageJ, cropped to eliminate background areas, and adjusted for contrast and brightness. In Avizo, the stack was then processed into 3D by tying the images slices together with image segmentation. The output was a 3D view of the core with changes in brightness over space corresponding to density contrast among different phases and pore structures in the core. The purpose of studying the image contrast was to identify mineralogy differences, vugs and high porosity areas connected by fractures, and to identify mineral precipitates in these areas. Regions of interest were later correlated with position along the core using the slice number and resolution (625 microns along a voxel edge). To detect subtle changes in density, the dataset was imported into Ilastik for segmentation into objects of varying brightness/intensity, color, edges, and texture using the software's algorithm. A single 2D slice was processed in an area of interest that contained a fracture, vug, and changes in mineralogy. Features in the black and white image were recolored based on their differences in these properties.

RESULTS

Comparative X-Ray Diffraction Analysis

Using XRD, the bulk composition of the three sidewall core trim samples above the oil-water contact and in a transitional region from oil-water were determined to be dolomite, while the sample from within the oil-water contact consists mainly of dolomite, calcite, quartz, and anhydrite. The core below the oil-water contact consisted of dolomite, anhydrite, halite, and sylvite.

Comparative Petrographic Analysis of Mineralogy, Fracture, and Porosity

The three thin sections of the trim samples were fully photographed with a Leica DMS 1000 digital light microscope and an Olympus SX50 polarizing light microscope to record changes in mineralogy, fractures, and pore spaces over the millimeter to centimeter scale. They were further analyzed in the SEM (for micrometer-scale observations). The high birefringence values of the major matrix minerals (dolomite and calcite) cause them to appear pastel colored in crossed polarized light. Photomicrographs of the thin sections often show air bubbles on the slides that were attributed to sample preparation. The blue material in the light optical micrographs is dyed epoxy that was used to impregnate the samples.

Above Oil-Water Contact: Trim 30 5588'

The trim sample collected from above the current oil-water interface displayed moderate porosity with some areas of high porosity near fractures. In the upper half and in the bottom right corner of the sample in **Figure 6**, the dolomite matrix thins out in a few isolated regions where blue epoxy shows through the more porous matrix. This section also shows different shades of brown in a low porosity area of the matrix. There are relatively few pores large enough to view with the digital light microscope. These are scattered across the slide and not correlated with large fractures. The pore distribution is generally heterogeneous. No intact frame building organisms were identified in the matrix, but recrystallization preserved remnant reef fabrics.

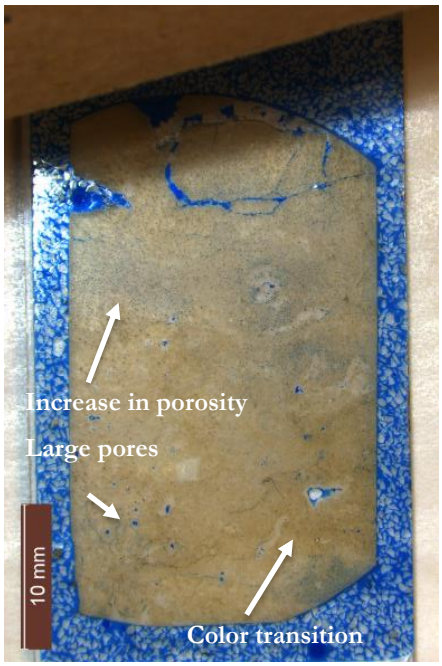

Figure 6. Low magnification digital light microscope image of trim sample located above the oil-water interface (depth 5588'). Observation of pores in this thin section is facilitated by the blue epoxy used to impregnate the sample. Darker shades of brown can be seen in some areas of the slide such as the lower right. In the lower right corner and upper half of the image, the sample displays a small increase in porosity, indicating a heterogenous pore distribution. A small number of pores large enough to see at this scale are found across the slide. These are not concentrated in low porosity areas, and they do not have a strong correlation with fractures.

There also are regions where the matrix abruptly transitions to a shade of off-white, indicating a change in mineralogy or texture in the matrix dolomite (**Figure 7**). These features are consistently present around areas of increased porosity and often are found as linings around larger pores. The ovoid shape in **Figure 7b** indicates that it is likely fossiliferous and preserves remnant reef fabric. At this magnification, the dark brown areas appear to be caused by clusters of small, dark grain sizes. Under the digital light microscope, these grains appeared very low in porosity, but they had boundaries of enhanced porosity. The polarized light micrographs in **Figure 8** displays the difference in grain texture and size compared to the fine grained matrix dolomite. In these images, the recrystallization to larger grain sizes is apparent against the fine grained dolomite. The central pores contain dark rims of either an opaque mineral or pyrobitumen, and organic material can be seen across the matrix.

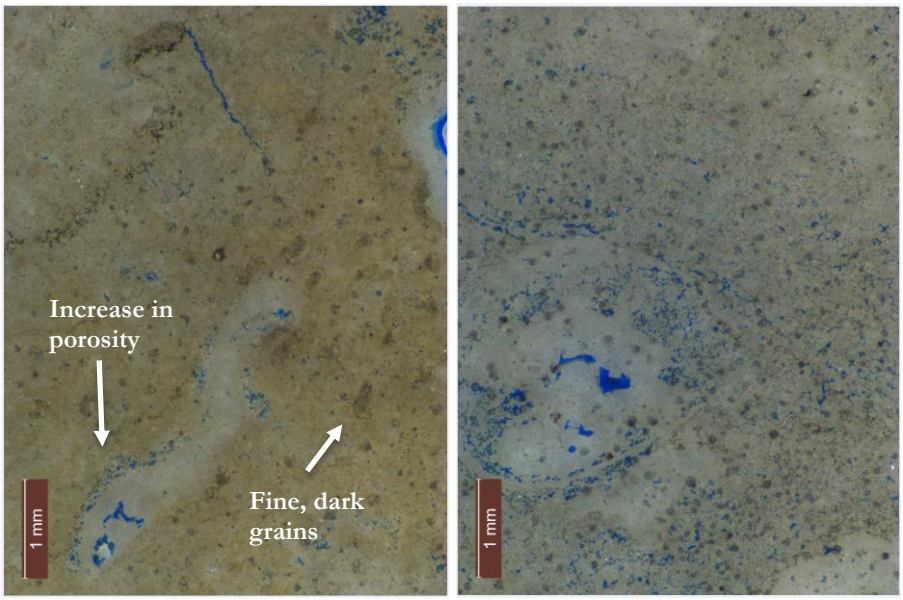

(a) **(b)**

Figure 7. (a) At left, a digital light microscope image showing abrupt changes in color and texture in the matrix. There is a solid white mineral with a distinct grain boundary adjacent to the relatively dark brown matrix. To the left of the feature, there is a thin chain of pores that follow this boundary with matrix dolomite In the upper right of the image, the white mineral creates a solid lining around a vug visible in **Figure 6**. (b) At right, a digital light microscope image of the white feature extending radially around large pores. Here, there is a local increase in porosity, and the lighter, solid mineral fills pore space in the center. This area appears to be a remnant reef fabric that was either dolomitized or filled with other fluids.

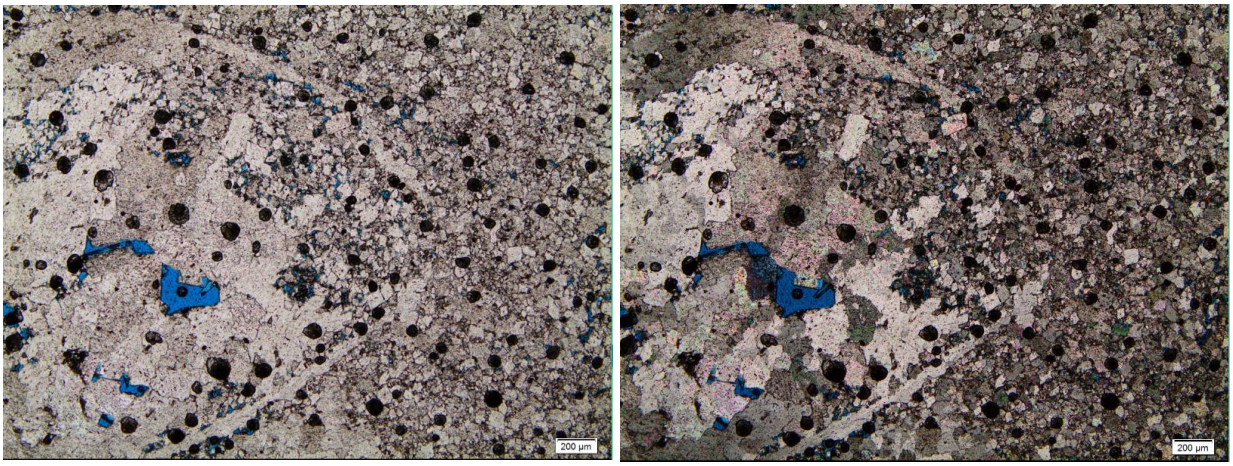

(a) **(b)**

Figure 8. Polarized light photomicrographs of the same area shown in **Figure 7b** in (a) plane polarized light and (b) and cross polarized light. Compared to the local matrix, the lighter mineral has few to no pores except the large central ones. The mineral has similar birefringence as the matrix, so it is likely recrystallized calcite or dolomite. Some of the larger pores contain dark rims consisting of either an opaque mineral or organic material, and spherical organic material is common across the matrix. Here, the pore spaces surrounding the recrystallized grains are harder to detect due to birefringence.

The 5588' trim sample also has a large, complex fracture system in the upper portion of the image **(Figure 9)**, which could be attributed to sample acquisition/preparation or pre-existing fractures. These open fractures disrupt the recrystallized white material and also branch out into the matrix in many directions, changing in aperture width across the section. The polarizing light microscope reveals many small, fragmented mineral grains from the matrix along the fracture systems in clusters and independent grains (**Figure 10**). These were located both on the edges of the matrix and in the void space. In this area, the aperture size was up to 0.3 mm in thickness. In cross polarized light these grains were the same pastel color of the matrix. Similar to the pore linings in **Figure 8**, these fractures and neighboring pore spaces commonly contained dark material (**Figure 11**).

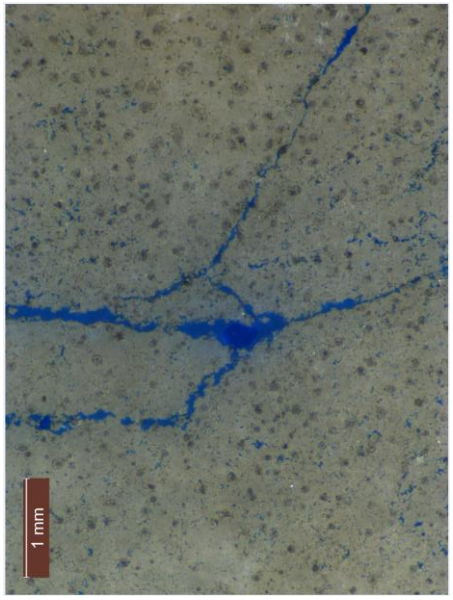

Figure 9. Digital light microscope image of a portion of a large, complex fracture system. Here, the fracture branches out in many directions and thins out from the center, disrupting large sections of the matrix (up to 3 mm long and 1 mm thick).

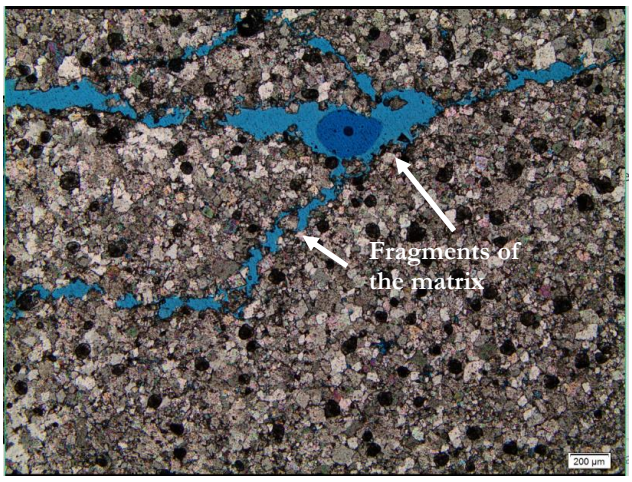

Figure 10. Polarized light photomicrograph of the large fracture system (cross polarized light), illustrating where the fracture has disrupted a section of the matrix shown in **Figure 9,** and almost entirely detaches it from the matrix on both sides. The void space of the fracture contains many fragments with the same interference colors as the matrix dolomite, so it can be assumed that these grains were originally part of the matrix.

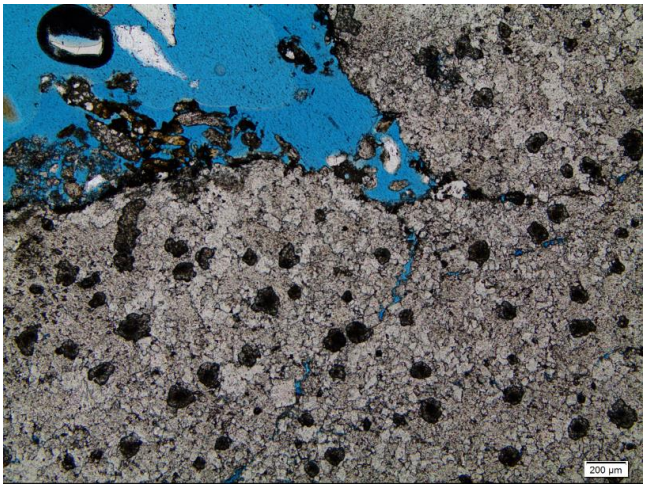

Figure 11. Polarized light photomicrograph of the large fracture in plane polarized light. Where the fracture extends into a thin branch to the right, the filling in the fracture appears darker and dirtier than the epoxy. The dark material is also present in the void space and along the edges. Similar inclusions of dark material are common along the other fractures and pore spaces in this sample. This is likely either pyrobitumen or an opaque mineral.

Thinner fractures also exist across the matrix of the 5588' trim sample that are filled with fine sediment (**Figure 12**). These fractures appear to cause offset and shearing of matrix textures and pore spaces, but they do not affect the recrystallized white carbonate. The recrystallized features appear to form along these fractures.

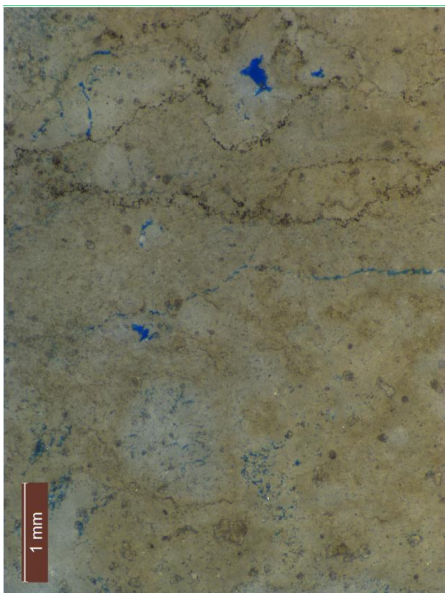

Figure 12. Thin, dark sediment filled fractures with a sharp to undulating toothed pattern in the matrix. In some areas these cause offset to preexisting matrix features, but the recrystallized matrix grains are not affected. Here, the recrystallized matrix grains are broken by open fractures.

Inclusions of potassium feldspar grains were found in multiple isolated areas of the slide with the matrix dolomite (**Figure 13**). These interlocked with the matrix dolomite, and contained inclusions.

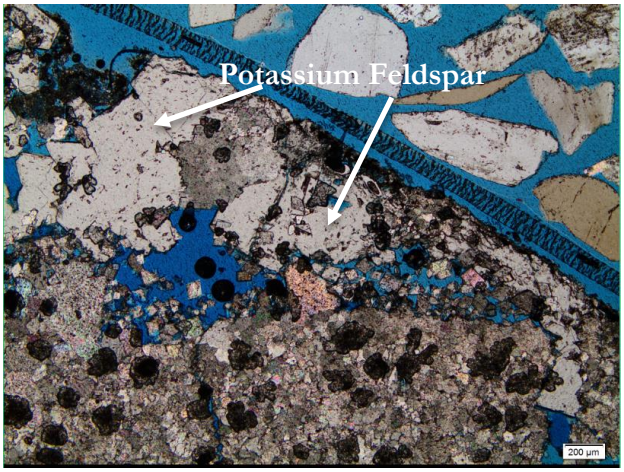

Figure 13. Plane polarized light photomicrograph of potassium feldspar in the matrix. These grains are interlocking with each other and with the matrix dolomite, and they appear to contain inclusions of other grains.

Oil-Water Contact: Trim 25 5630'

The trim sample collected from within the current oil-water interface displayed a heterogeneous pore distribution. In **Figure 14**, the sample displays moderate porosity in the bottom half and relatively high porosity in the top half of the image. The portion in the top of the image contains many large pore spaces, and at high magnification, some appear to be stained by organic material (**Figures 15 and 16**). Small droplets of organic material is common across the matrix. Similar to the previous sample (5588'), this sample contains large areas where the color is darker brown. But, unlike the previous sample, these occur both in areas of high and low porosity. The matrix of this sample is primarily dolomite with minor calcite and accessory minerals such as quartz and anhydrite (determined with XRD). There are not remnant fabrics from reef-building organisms observed in this section, so dolomitization must have replaced them.

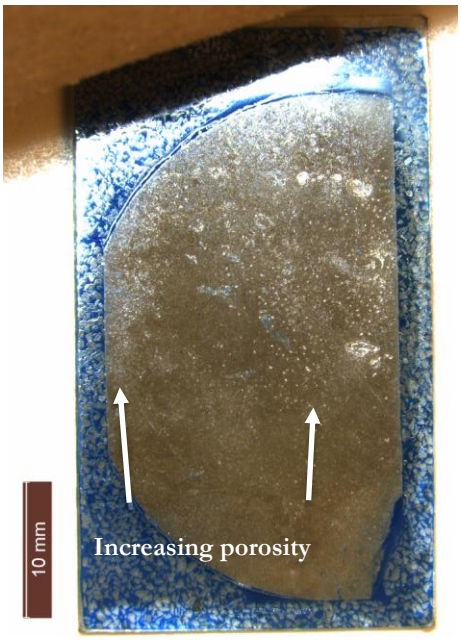

Figure 14. Low magnification digital light micrograph of trim sample located within the oil-water interface (depth 5630'). Regions of increasing porosity are shown with the white arrows (toward the top and left edge of the image). Roughly half of the section contains few to no pores visible at this scale, and half shows relatively high porosity with a wide range of pore sizes. The matrix displays two shades of brown across the slide possibly due to changing organic content.

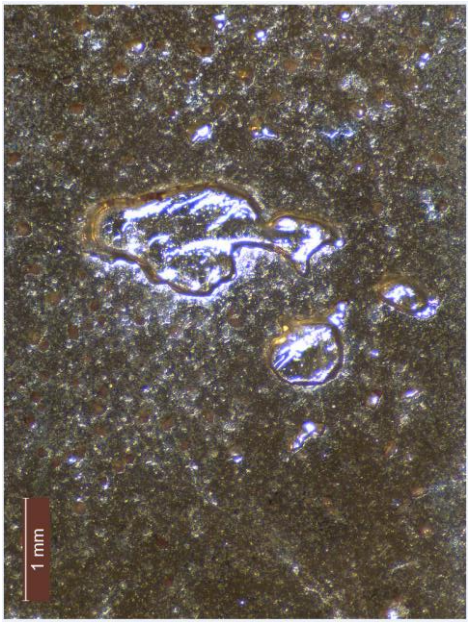

Figure 15. Digital light micrograph of large porous areas stained by organic matter. Many pores in the slide have dark brown rims similar to this one. Pores measure to about to 1 mm.

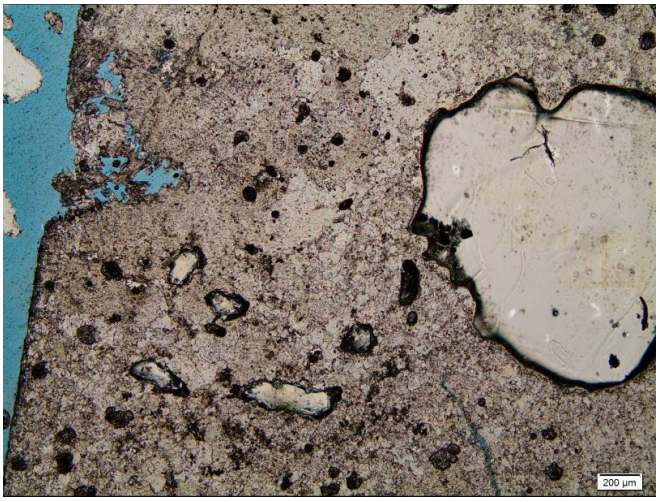

Figure 16. Polarized light micrograph of large pores stained with organic matter or lined with an opaque mineral in plane polarized light. There are many pores with dark rims around the edges, and similar dark features can be seen in the calcite/dolomite matrix as well. It is unknown why the pores appear to contain a white film.

Figure 17 displays the only facture visible at this scale (lower left region of **Figure 14**). This fracture is thin, and no aperture is visible except with the SEM. However, more micro-fractures can be seen with the polarized light microscope (**Figure 18**).

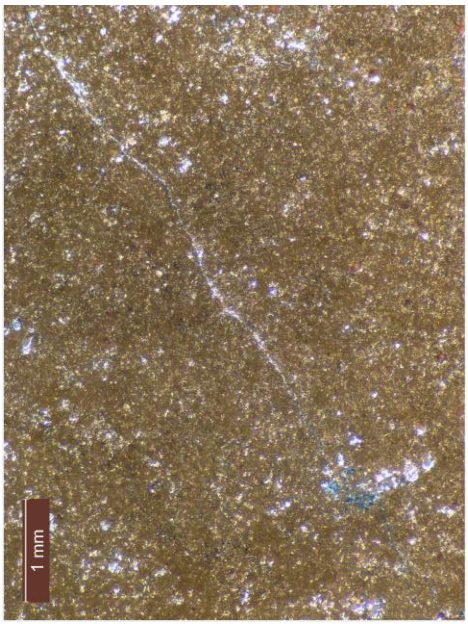

Figure 17. Digital light microscope image of the only fracture visible at this resolution (depth 5630'). With SEM analysis, some matrix dolomite,calcite fragments and organic material are observed filling the fracture. Open fracture apertures are present but discontinuous.

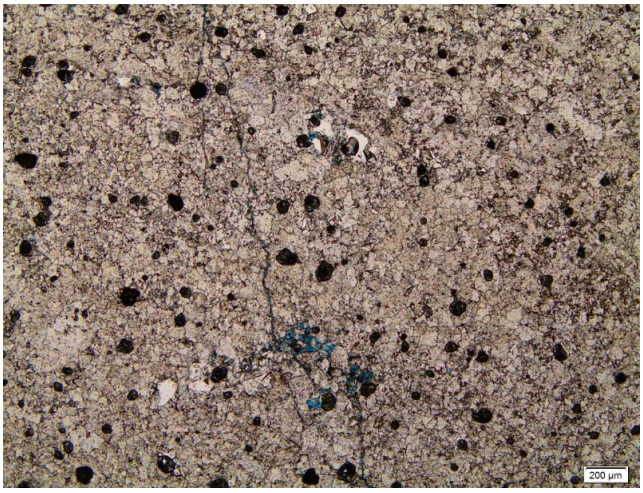

Figure 18. Polarized light micrograph of the fracture shown in **Figure 17**. Here, the fracture appears to be a complex system of microfractures connecting small pores in the calcite/dolomite matrix. At this scale, discontinuous blue epoxy can be seen in the thin aperture. Most the of fracture is filled with calcite and dolomite.

Using the polarized light microscope, changes in birefringence displayed accessory minerals that still need to be identified (**Figure 19**). These commonly show first order interference colors and could be gypsum, quartz, or anhydrite.

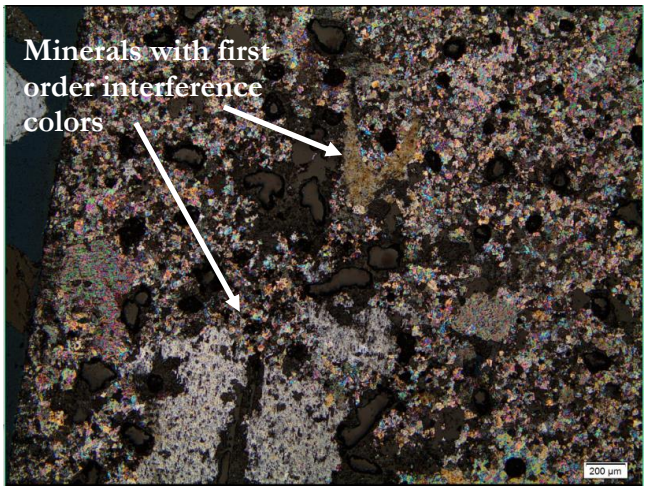

Figure 19. Polarized light photomicrograph taken in cross polarized light of minerals with low birefringence. These accessory minerals are common within the matrix and have first order interference colors. These grains could be the quartz that was identified with XRD or evaporites that are common in the reefs.

Transition Zone: Trim 20 5655'

The trim sample collected from the transition zone from oil to water displayed heterogeneous porosity in the dolomite matrix. Similar to the oil zone, there are nonsystematic distributions of moderate porosity and high porosity. Porosity is low in portions near the center of **Figure 20**, but increases towards the left, right, and top edges of the image. There are several large pore spaces across the slide with irregular shapes. This sample also contains many areas where the color changes to darker brown (**Figure 21**). In this sample, the color changes in smaller clusters in areas of lower porosity. Organic material can be seen across the matrix.

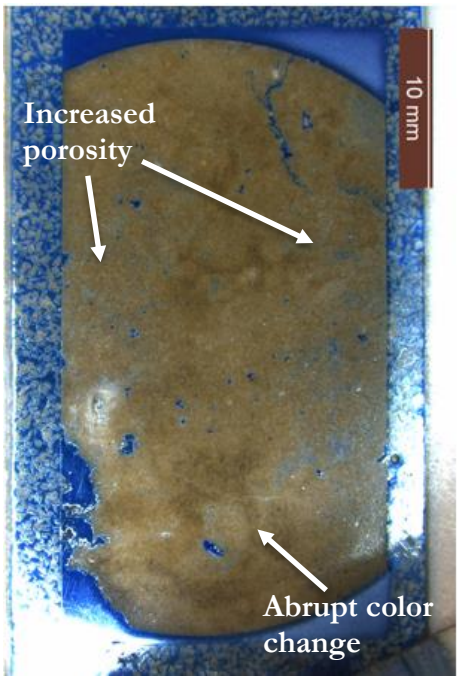

Figure 20. Low magnification digital light microscope image of trim sample located within the transitional zone from oil to water (depth 5655'). There some small regions of low porosity with varying shades of brown, but porosity increases more towards the edges. Several large pores are observed in areas of increased porosity and around the fractures. The dark brown tends to be absent in these areas.

Figure 21. Plane polarized light micrograph of a dark brown portion of dolomite matrix. Here, brown specs and stains in the matrix that may be organic material.

Two fractures are visible in the upper right portion of **Figure 20**, but at higher magnifications these are observed to be connected. The larger branch of the fracture is shown in **Figure 22** and contains clusters of grains in the void space. At higher magnifications, these grains are observed in clusters and independently as many small, fragmented minerals (**Figure 23**). They are located both on the edges of the matrix and suspended in the void space. In cross polarized light these grains are the same pastel color as the matrix. The fracture system extends across the upper right region of **Figure 20**. The fractures connect pore spaces and show a lot of detachment of matrix grains.

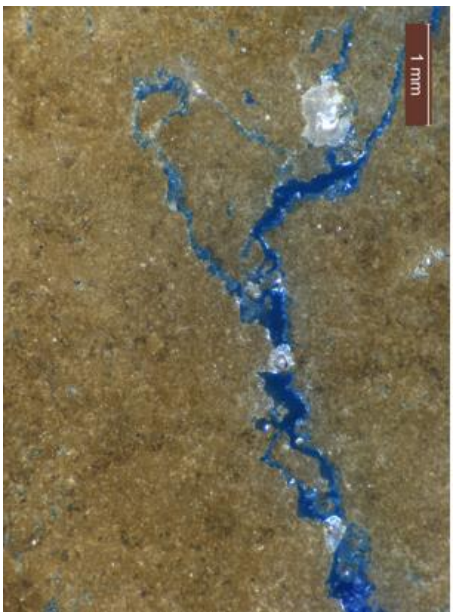

Figure 22. Digital light micrograph of the large fracture, measuring about 8 mm long in this section. There appears to be a light blue lining along the edge of the fracture as it transitions from dark blue

void space to brown dolomite rock. This could possibly be new material or stained dolomite matrix fragments. The void space of the fracture contains large groups of grains up to 1.2 mm long that are detatched from the matrix.

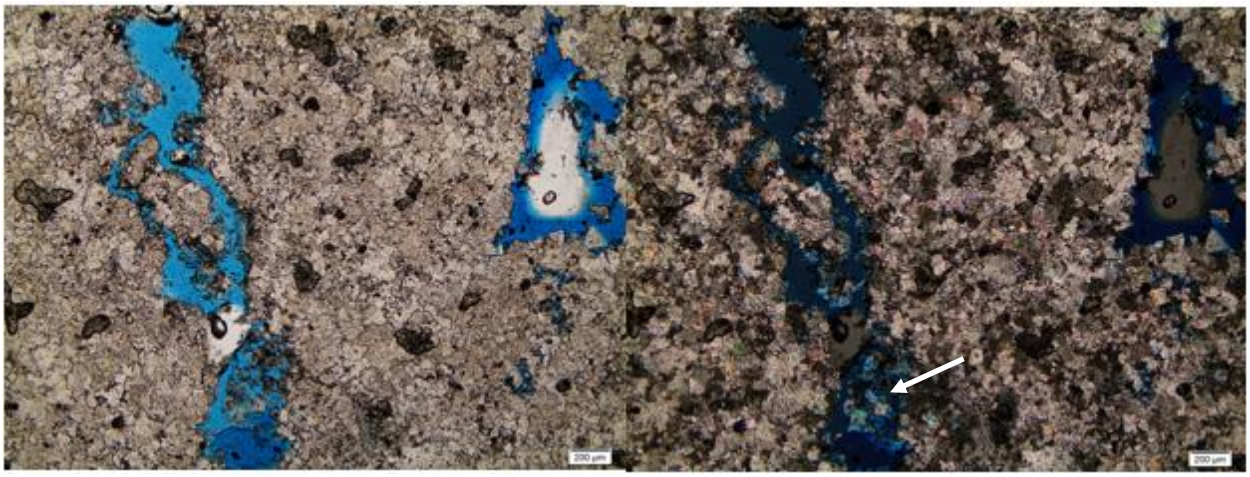

Figure 23. Polarized light micrographs of the center of the large fracture in plane polarized light (a) and cross polarized light (b). There is a cluster of large, fragmented dolomite grains in the center of the fracture. Many small grains are dispersed along the edge of the matrix and in void space. Cross polarized light shows some minerals have similar birefringence as the matrix. On the right side of the images, there is a relatively large pore space (about 1.2 mm tall and about 0.6 mm wide) with that appears to be connected to the large fracture with a micro fracture. This pore contains some light blue material. Small, dark inclusions along the fracture and in the pore space are either organic material or an opaque mineral.

The matrix also contains reef fabric as shown in **Figure 24**. The remnant fossil appears to be the same composition as the matrix, but has a different texture. It creates a distinct boundary of recrystallized material against the matrix.

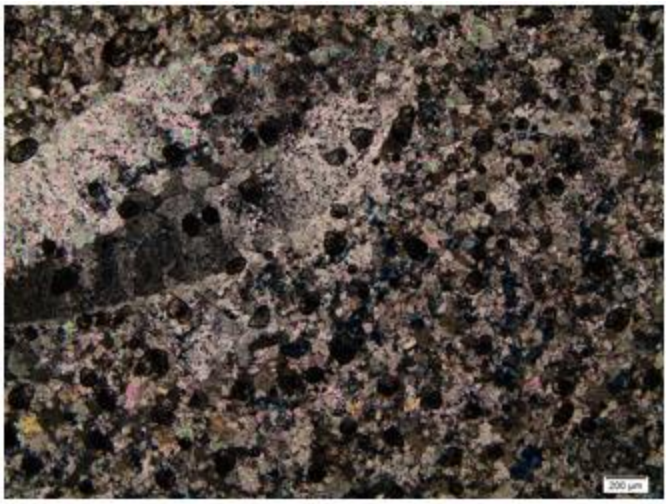

Figure 24. Polarizing light microscope image of an ovoid fossil against the matrix dolomite. The birefringence appears the same as the dolomite, but the grains are in optical continuity, are much coarser, and lack porosity. This suggests the area was leached and recrystallized with carbonate minerals, either dolomite or calcite.

A large pore in the sample (almost 2 mm wide) contains a relatively large anhydrite grain (**Figure 25**). The grain is about 0.5 mm long and precipitated from the edge of the dolomite matrix into a pore. The anhydrite was identified by its change in interference colors, and its elemental composition was confirmed in the SEM.

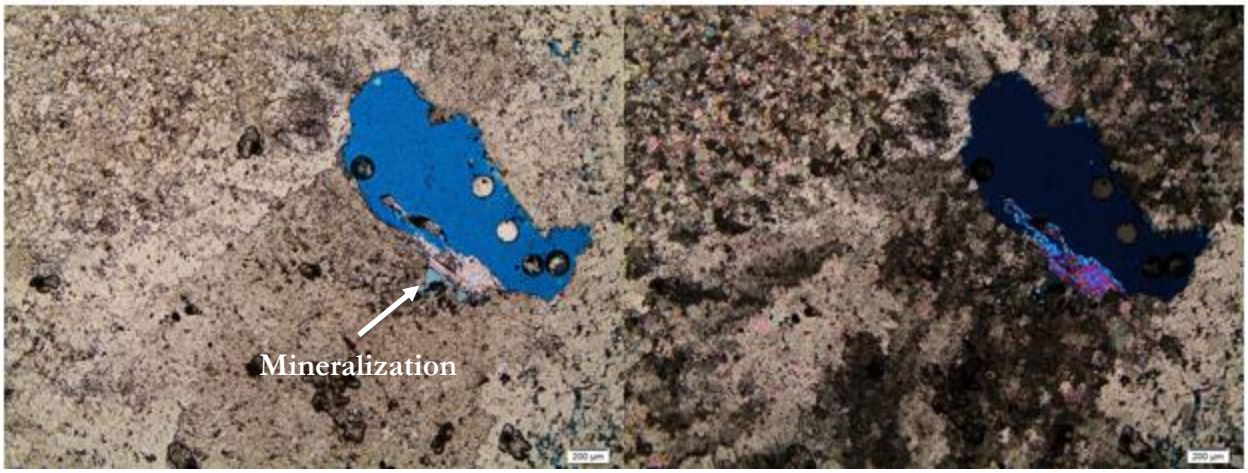

Figure 25. Polarized light micrographs show mineralization along matrix/vug grain boundaries (arrowed) in plane polarized light (a) and cross polarized light (b). The birefringence observed in (b) is consistent with anhydrite. This pore is large enough to see in low magnification the digital light micrographs. Surrounding the pore, there is a local increase in porosity and abrupt absence of dark brown.

SEM analysis of Mineralogy, Fracture, and Porosity

Using SEM, changes in mineralogy, fractures, and pore spaces of the three thin sections were observed at the micrometer scale. The epoxy in the trim samples appears dark and smooth in SEM images. By using EDXS in the SEM, most minerals were able to be identified in the samples. Pores with sharp, euhedral boundaries are abundant across the matrix. These pore shapes are due to the crystallographic directions of the dolomite matrix and contained mineral inclusions. One mineral consistently found in the pores of the dolomite matrix was a high magnesium carbonate that differed in both magnesium and oxygen concentration as compared to matrix dolomite. Other pores consistently contained epoxy, pyrobitumen, and evaporites.

Above Oil-Water Contact: Trim 30 5588'

Smaller fracture systems and grain boundaries can be seen under higher magnification in the SEM (**Figure 26**). Around the fractures, there are infillings of the high magnesium carbonate. In the apertures, dolomite mineral grains are commonly detached by the same angular geometry that the pores exhibit, but there are areas where the grain boundaries are anhedral.

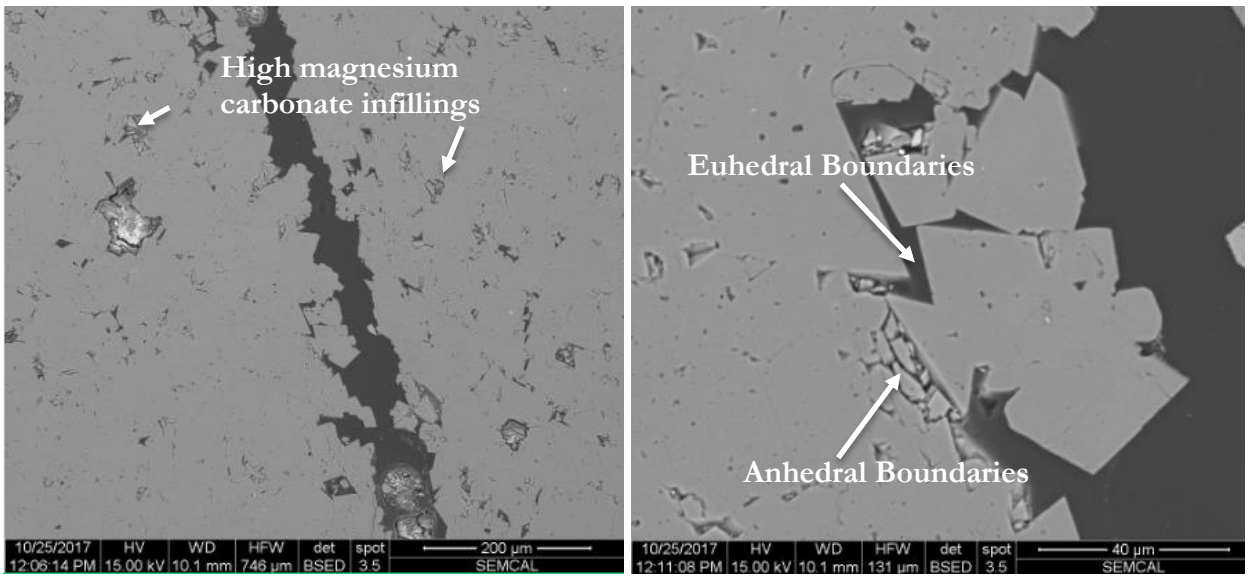

Figure 26. (a) At left, a backscattered SEM image taken along the large fracture system with adjacent angular pore spaces. Some pores include infillings of the high magnesium carbonate. (b) At right, a magnified view of disrupted mineral grains. The blocky grains are dolomite detached from the matrix along its crystallographic directions. Grains along the fracture are broken with both euhedral and anhedral boundaries.

SEM analysis allowed for improved detection of accessory minerals that are not observed with XRD. For example, **Figure 27** shows potassium feldspar embedded in matrix dolomite. These grains often existed with euhedral dolomite inclusions. Fluorite (**Figure 28**) was also found in the matrix and contains interstitial dolomite grains. Organic material (**Figure 29**) is observed in both matrix and pores. Barite-celestite grains were also identified in pore spaces.

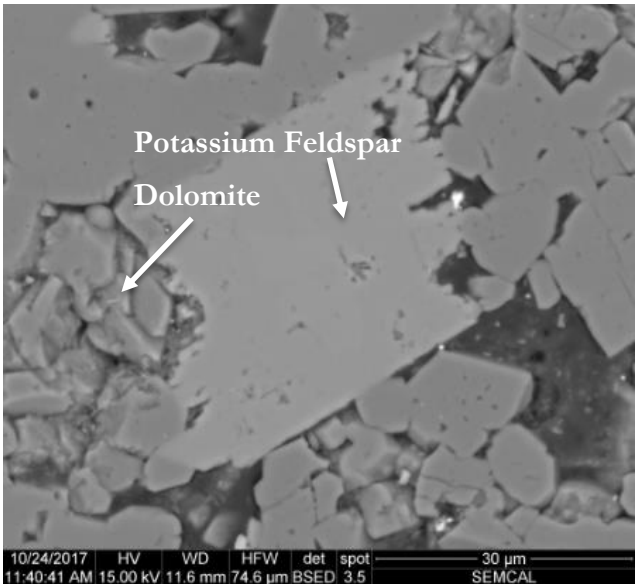

Figure 27. Backscattered SEM image of potassium feldspar adjacent to a vuggy pore containing dolomite. The potassium feldspar grain cleaves in a different geometry than the dolomite, and displays a brighter BSE signal intensity. Some potassium feldspar grains contained euhedral dolomite inclusions.

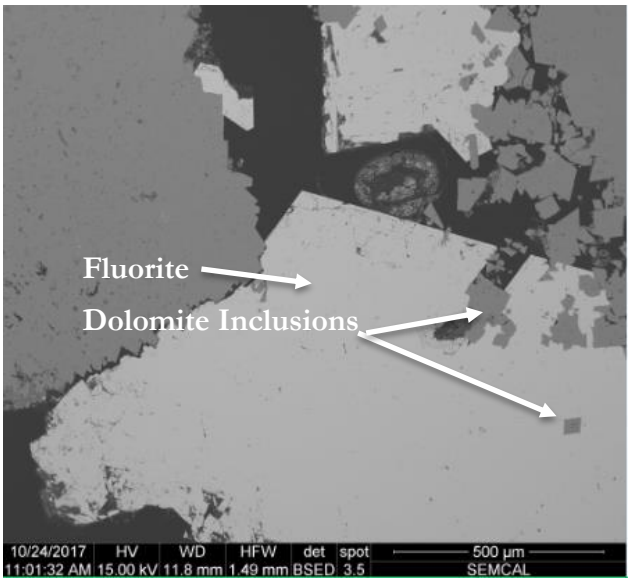

Figure 28. Backscattered SEM image of a fluorite infilling in a vuggy matrix region. The brighter mineral is fluorite and the darker gray mineral is dolomite. The fluorite contains inclusions of dolomite.

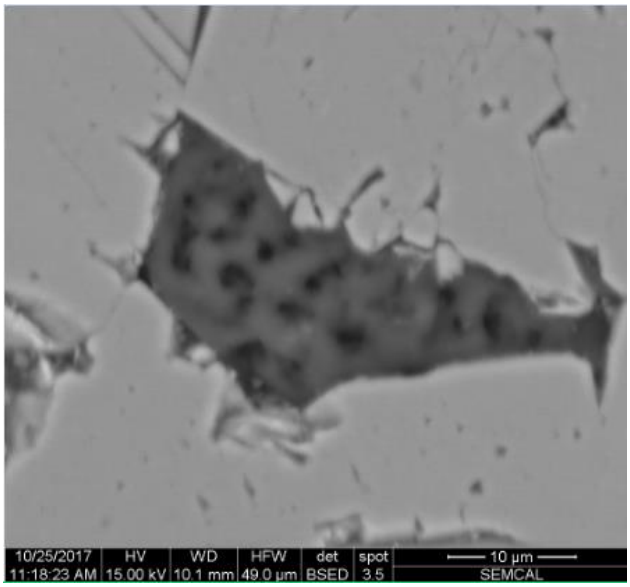

Figure 29. Backscattered SEM image of organic material filling an angular pore space surrounded in the dolomite. The texture is different than that shown by epoxy, which appears smooth and dark in void spaces. As viewed with BSE, the organic material varies in gray scale and has uneven texture. This area displays the common pore shape due to the crystallographic directions of dolomite.

Oil-Water Contact: Trim 25 5630'

Similar to the previous sample, there are many pores with sharp, angular boundaries (**Figure 30**). These are tend to be larger and more abundant in the oil zone. These pores often contain the high magnesium carbonate precipitating from the matrix dolomite/calcite in a different orientation (**Figure 31**). The pores also contain inclusions of salts (**Figure 32**) and organic material (**Figure 33**). As detected with XRD, quartz is present as an accessory mineral (**Figure 34**) along with fluorite and pyrite. Phyllosilicate was also observed with SEM, but not detected with XRD.

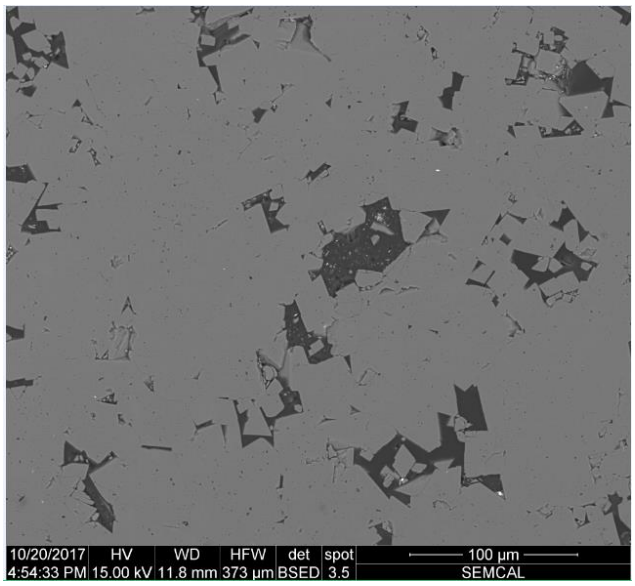

Figure 30. Backscattered SEM image of the common angular-shaped pores created from euhedral matrix dolomite/calcite. The poreshape often are infilled with organic material and minerals such as the high magnesium carbonate, evaporites, and fluorite. Pores are large and abundant in the porous half of the sample.

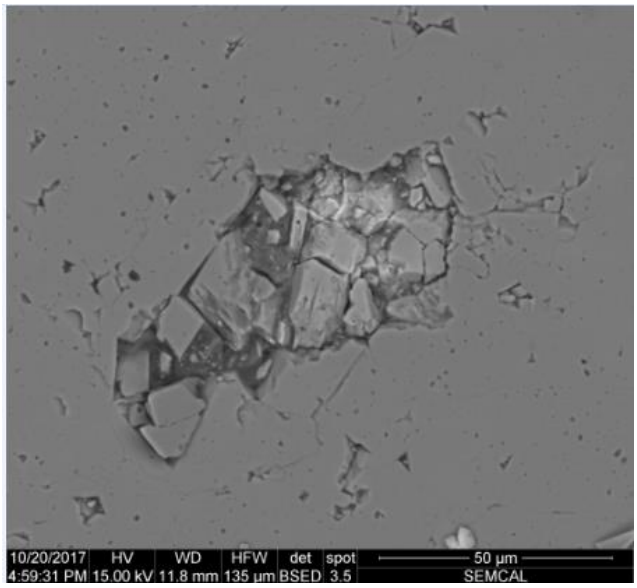

Figure 31. Backscattered SEM image of the high magnesium carbonate mineral precipitating within the matrix dolomite. The mineral is bound by the angular pore shape, but the infill material has a different orientation than the matrix material, indicating it is from another generation.

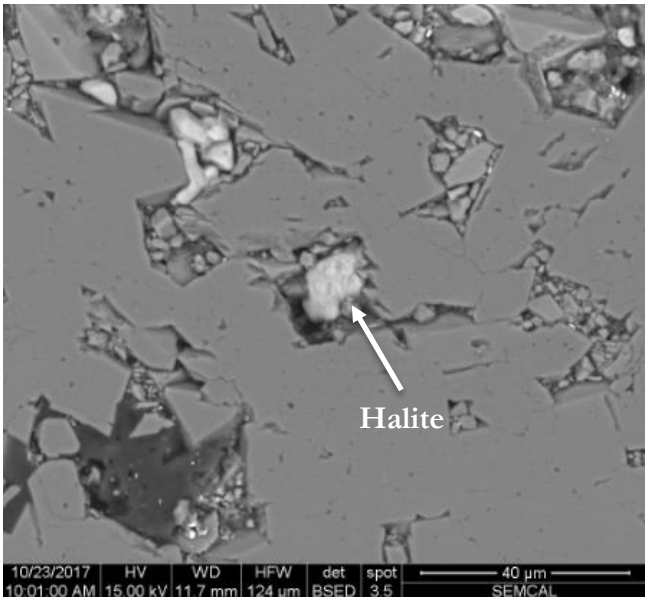

Figure 32. Backscattered SEM image of salts filling pore spaces in the dolomite matrix. The bright white salt in the center is halite, identified with EDXS.

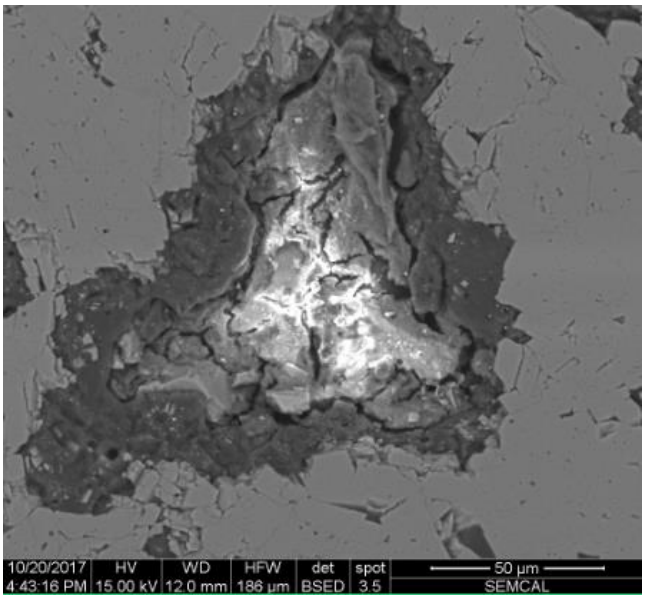

Figure 33. Backscattered SEM image of a pore containing organic material. This material appears rough and thick as opposed to smooth epoxy. The light material in the center is likely carbonate charging in the electron beam.

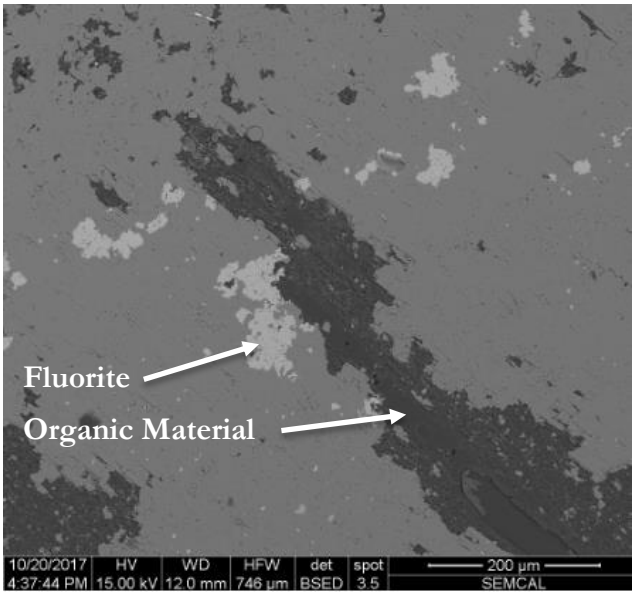

Figure 34. Backscattered SEM image of fluorite as an accessory mineral in the medium gray dolomite matrix. The dark material in the pore space is likely more pyrobitumen. Here, fluorite is relatively abundant.

Transition Zone: Trim 20 5655'

The fracture system in this sample is extensive and consists of many smaller branches of fractures. These connect to pore spaces and are associated with a lot of damage and detachment of matrix dolomite. These connected pore spaces are commonly filled with the high magnesium carbonate (**Figure 35**).

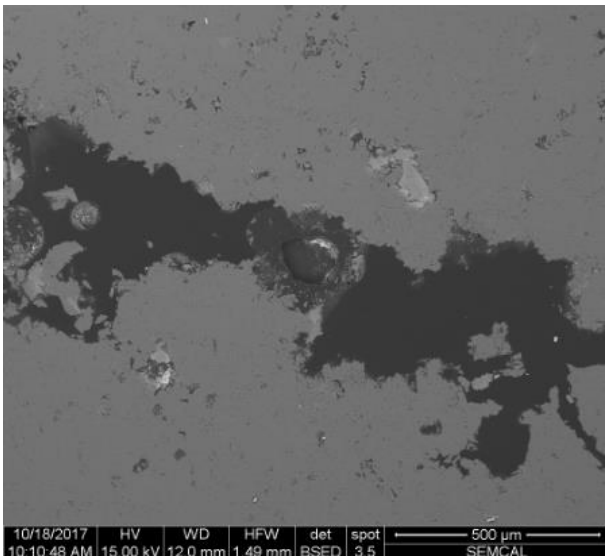

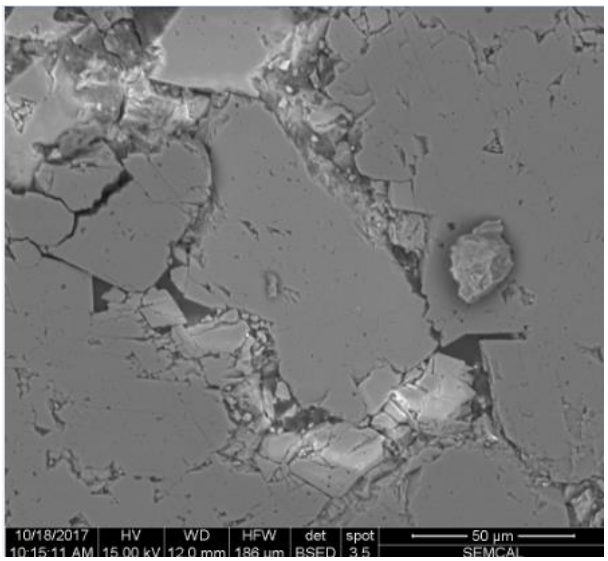

Figure 35. a) At left, a backscattered SEM image of part of the large fracture system. Small mineral grains line the matrix, and some are suspended in epoxy. Thinner fractures branch out from the core of this fracture system, and connect pore spaces. b) At right, an SEM image of a zoomed in view of a connected infill. This shows a connected pore space that has been infilled by the high magnesium carbonate mineral.

Similar to the other two samples, there are many pores with sharp, angular boundaries across the section. The pores contain inclusions of anhydrite (**Figure 36**), calcium chloride and organic material (**Figure 37**), salts (**Figures 38, 39**), fluorite (**Figure 40**), sulfides (**Figure 41**), and most commonly, a high magnesium carbonate (**Figure 42**). All of these minerals precipitate in the pores of the dolomite in different orientations, suggesting formation at a later generation.

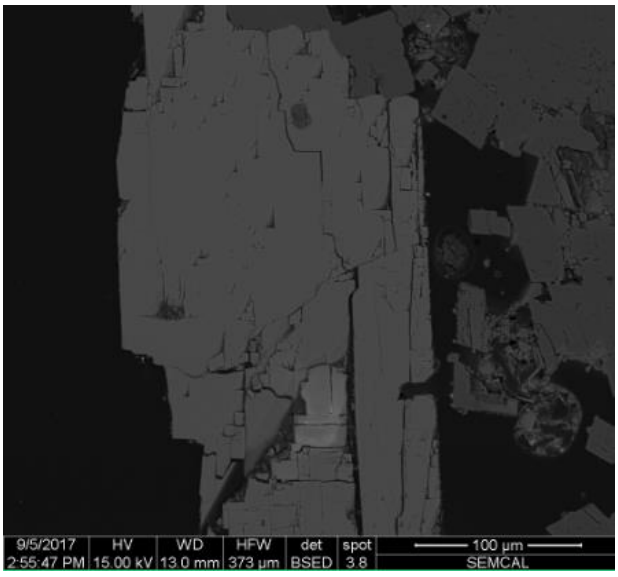

Figure 36. Backscattered SEM image taken of the bright interference colored mineral seen with the polarizing light microscope. The EDXS chemical composition was consistent with anhydrite. The grain is attached to the dolomite matrix, extending out into the void space. The boundaries of the matrix in this large pore space are not consistent with the smaller pores with angular, euhedral boundaries.

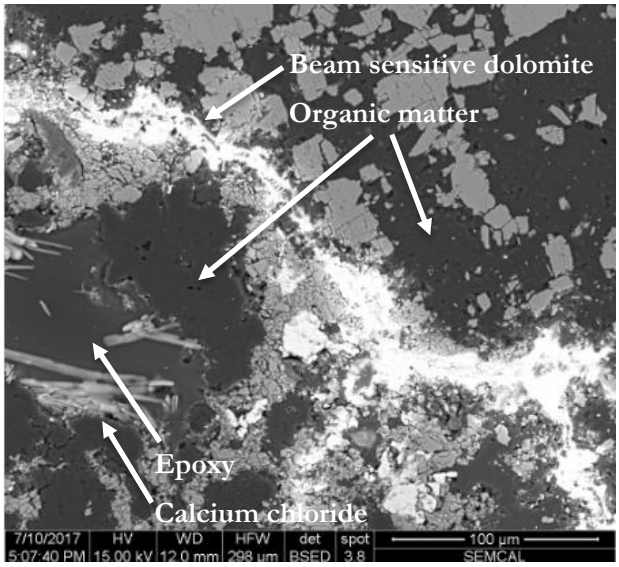

Figure 37. Backscattered SEM image of a vug in dolomite matrix containing anhedral grains of beam sensitive dolomite (bright white), organic matter, and calcium chloride. The vug contains two distinct textures in the dark void space. The smoother texture is the epoxy, and the adjacent texture is likely organic matter. The needle shaped crystals in the void space are calcium chloride, which likely form as salts precipitate from pore water during sample preparation.

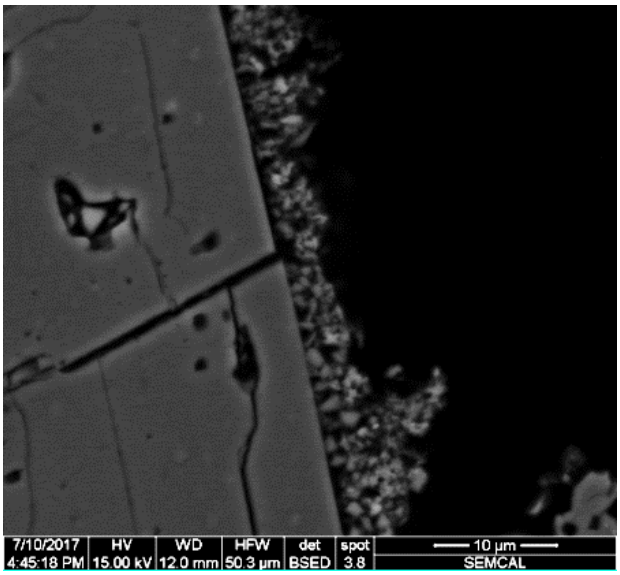

Figure 38. Backscattered SEM image of salts lining the matrix dolomite in a pore space. The brightness and contrast of this image were each increased by 40% due to the darkness of the original image.

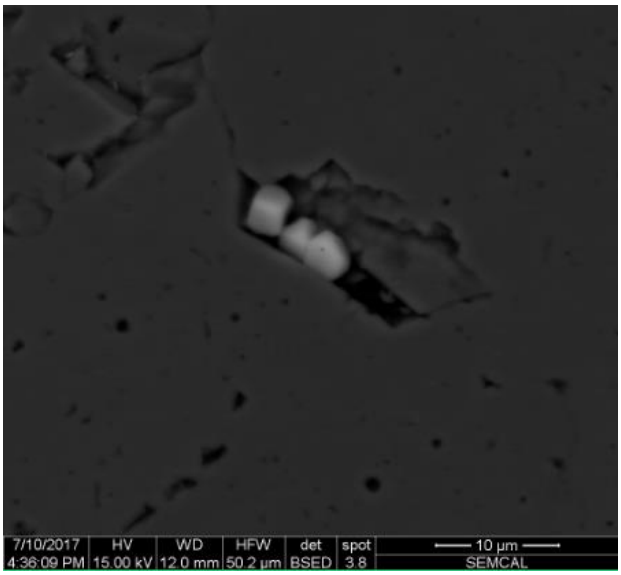

Figure 39. Backscattered SEM image of cubic salts (either halite or sylvite) that filled a pore space in the matrix dolomite.

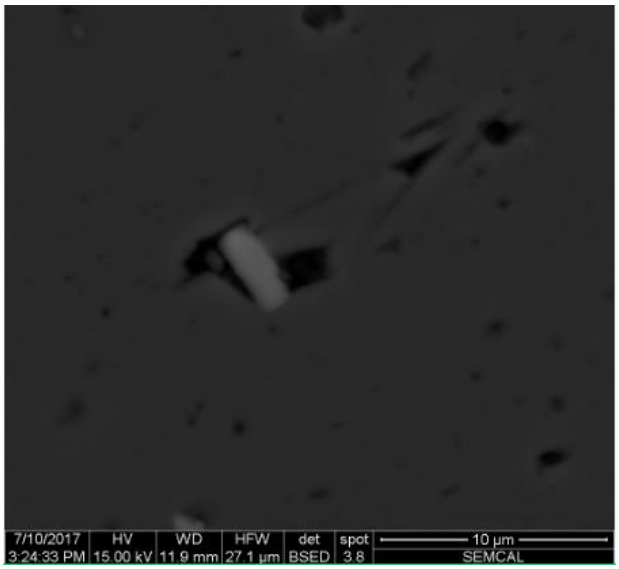

Figure 40. Backscattered SEM image of fluorite partially filling a pore in matrix dolomite.

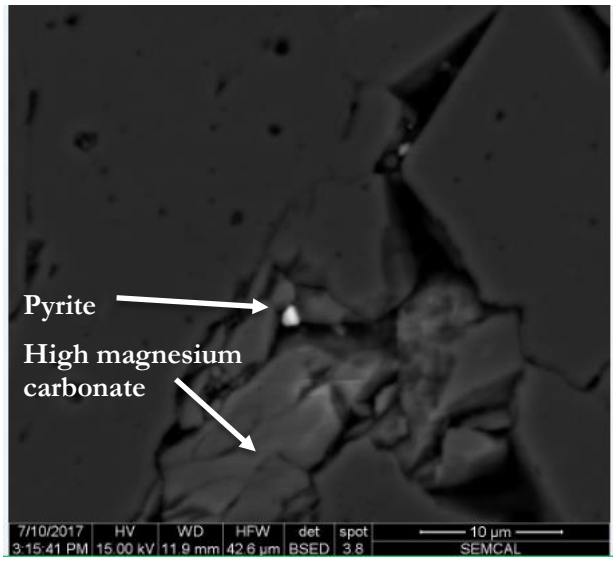

Figure 41. Backscattered SEM image of a sulfide, probably pyrite, in a matrix pore. The bright white mineral is the sulfide, and the rest of the pore filling is the high magnesium carbonate.

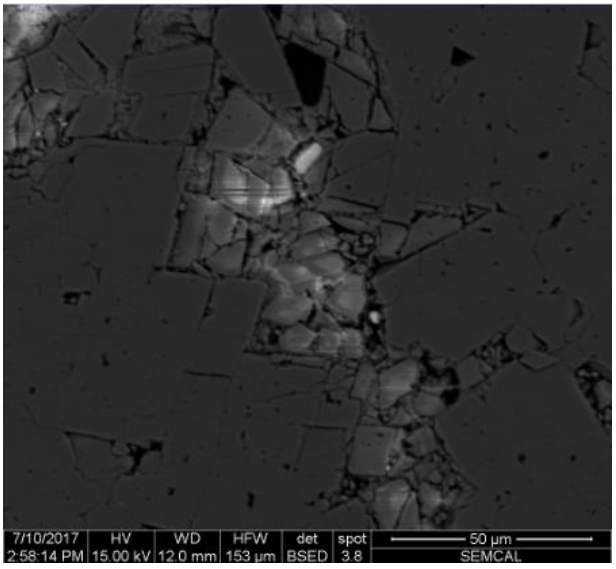

Figure 42. Backscattered SEM image of the high magnesium carbonate filling a pore and bounded by the matrix dolomite. Here the pore space is almost completely occupied.

XCT Scan and Pixel Classification Analysis

XCT and micro XCT scans of the core sample from depth 5690', which is below the current oil-water interface, were analyzed after 3D rendering. **Figure 43** shows two views of a large, relatively low density, rhombohedral mineral bounded by the higher density matrix. Adjacent slices showed natural fractures connected to this vug. The micro XCT scans of the corresponding position on the

core were analyzed at higher resolution and segmented by an algorithm in Ilastik (**Figure 44**). This process re-colored (segmented) the selected image slice based on both brightness and shape. The output was a new image that labeled the rhombohedral mineral yellow, void spaces red and dark red, an accessory mineral as green, and the matrix as purple and blue. SEM and XRD measurements were needed to identify the composition of this area. The core matrix is dolomite, whereas the material hand-picked out of this vug consists of mostly dolomite and anhydrite with minor halite, sylvite, and calcium chloride salt.

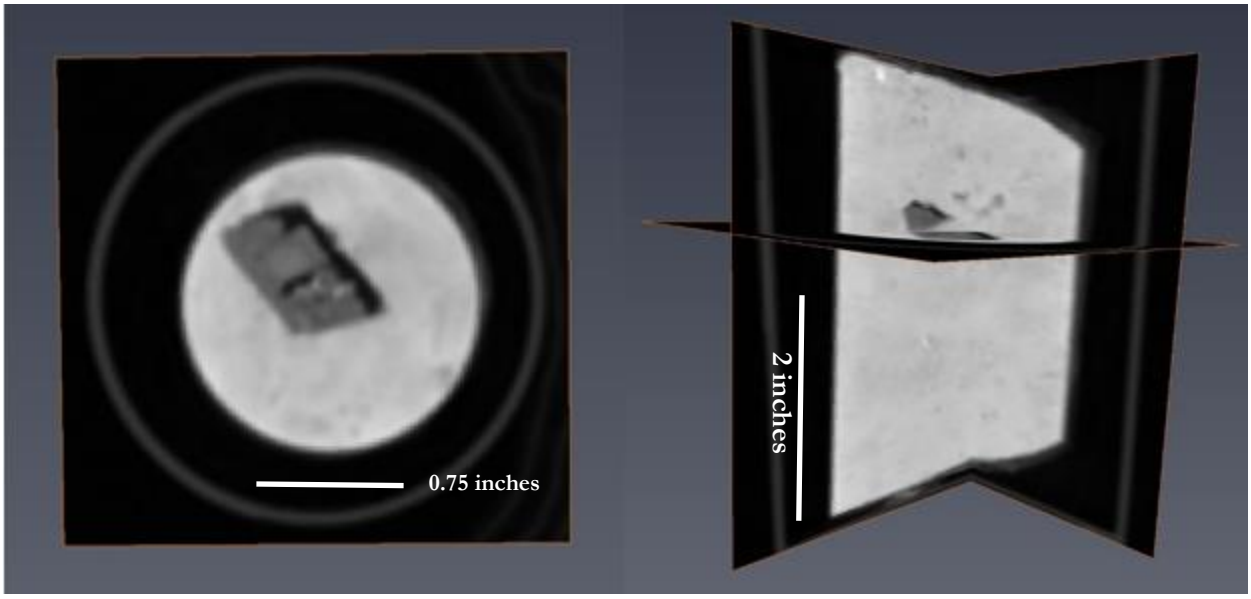

Figure 43. a) At left, an XCT scan slice of the core 5690' showing the secondary mineralization of within a rhombohedral pore in dolomite matrix. b) At right, an edge on view of the slice, locating the mineralization about 1/3 of the way down along the length of the intact core. Using the slice number and the 625 micron voxel edge, this feature's position on the core can be calculated.

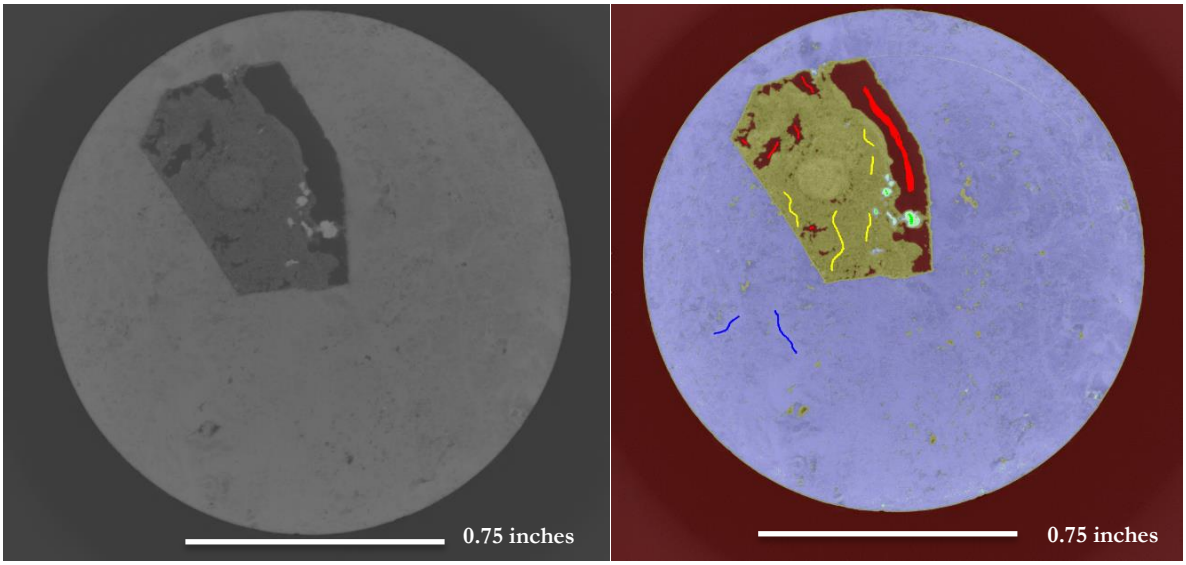

Figure 44. a) At left, a micro XCT scan of the core from the corresponding position as **Figure 39**. b) At right, the output image from Ilastik where the low-density mineral is recolored yellow. The pore contains some void space to the right of the mineral (red), and the mineral is bound by the purple matrix. The green accessory minerals were determined with XRD to be a sulfide.

Discussion

Summary of Results

Rock properties of carbonate samples from a Dover well in Otsego Co., MI were analyzed to assess how mineralogy, porosity, and fracture attributes compare with depth. **Tables 2** and **3** summarize results for each sample acquired from the reservoir rock. There are no significant changes in porosity from above the oil-water contact to below the oil-water contact. Each sample had a heterogeneous pore distribution with moderate and higher areas of porosity and similar pore shapes. Generally, there were more salt inclusions and less organic inclusions below the oil-water interface. Below the oil-water contact, only one pore and fracture area were analyzed in this study, so general conclusions were not made. There is not a systematic relationship between location in the reservoir and fracture size or amount of fractures. In the oil zone and in the oil-water interface, organic material is more common in fractures. Fractures in every sample contained fragments of its matrix. Below the oil-water contact, only one pore and fracture area were analyzed in this study, so general conclusions were not made.

Table 2. General porosity, pore sizes, fillings, and shapes for each sample.

Depth (ft.)	Reservoir Location	Porosity	Pore Sizes	Pore Fillings	Pore Shapes
5588'	Above oil-water contact	Heterogeneous, Moderate and high	Most on the mm to μm scale	High Mg carb, salts, fluorite, barite-celesetite, organic material	Euhedral and anhedral
5630'	Within oil-water interface	Heterogeneous, Moderate and high	cm to μm scale	High Mg carb, halite, organic material	Euhedral and anhedral
5655'	Transitional region from oil to water	Heterogeneous, Moderate and high	Some on the cm scale, most on the mm to μm scale	Anh, high Mg carbonate, salts, fluorite, sulfide, organic material	Euhedral and anhedral
5690.25'	Below oil-water contact			Dol, anh, halite, calcium chloride, sulfide	Euhedral

Table 3. Fracture types, filling minerals, and aperture size for each sample.

Depth (ft.)	Reservoir Location	Fracture types	Filling Minerals	Aperture Size
5588'	Above oil-water contact	One large system, stylolite fractures	Dolomite, organic material., fine sediments	Up to .3 mm
5630'	Within oil-water interface	One small system	Dolomite, cc, organic material	Discontinuous, µm scale
5655'	Transitional region from oil to water	One large system	Dolo	Up to 1 mm
5690.25'	Below oil-water contact	At least one fracture system connecting to a vug		

Although these samples originated from different depths of the reservoir, there were common sample characteristics. Most pore spaces were angular with sharp, euhedral boundaries due to the crystallographic directions of the matrix dolomite. Relatively large pore spaces and areas along fractures sometimes deviated from this pattern, containing some minerals with anhedral boundaries. This could be due to dissolution and the shape of original reef fossils. Pore spaces that contained inclusions of minerals with different geometries and compositions than the matrix were abundant, which indicates they formed in a later generation. Commonly precipitating in these pores were the high magnesium carbonate and evaporite minerals. Each sample also contained organic material, likely pyrobitumen. This commonly existed as spherical hydrocarbon droplets across the matrices. Porosities and fractures didn't vary systematically with placement in the reservoir. However, the oil zone and oil-water interface generally exhibited more complex matrix compositions than the deeper regions of the reservoir, and their pores and fractures contained more organic material and less salt. The complex mineralogies could have been caused by reef and detrital material. These samples could have come in contact with off-reef material if they originated from the windward side of the reef. Destruction of the original reef fabric makes this correlation difficult.

Diagenesis, Brine Evolution, and Implications for Rock Properties

Early diagenesis in the northern reef belt was initiated by dolomitization of the calcite/aragonite reef to dolomite (Cercone and Lohmann, 1987). This destroyed the reef fabric by leaching the matrix and increasing porosity. Minor calcite remains in the reservoir rocks as detected with XRD and SEM, but there is very little remnant reef material preserved in these samples. The destruction of reef organisms makes correlation between samples and facies models difficult. The Niagaran and A-1 carbonate formations consist of the reef core and tidal flat environments, respectively, but correlation can't progress without knowledge of the organisms and position in the reef. In the oil

zone and in the transitional zone, small ovoid shapes were preserved and visible by microscopy. The textural and compositional details of the fossils were not preserved, and the material had been recrystallized to calcite or dolomite. Detection of calcite in the oil-water contact could be attributed to a lower degree of dolomitization. The dolomitization allowed for better reservoir potential by increasing porosity and vug volume. It was caused by early subaerial exposure of the reefs and reflux of hypersaline brines during shallow burial (Cercone and Lohmann, 1987). Porosity did not drastically differ with reservoir depth, but small differences could be due to degree of subaerial and brine exposure or amount of fossil content. Irregular pore shapes may be attributed to ancient fossil shapes. Subsequently, evaporite precipitation initiated second generation growth in pore spaces. However, due to the location of this reservoir on the ramp, large amounts of salt plugging did not occur, and porosity was not reduced to the point of eliminating reservoir potential. However, this would account for the small salt inclusions in the pore spaces throughout the reservoir.

Over time pressures and temperatures increased with burial and depth, which initiated hydrocarbon generation in the Mississippian and subjected the rocks to hydrothermal alteration. Late diagenesis is onset by stylolite fracturing and partial dissolution in the lower reefs (Cercone and Lohmann, 1987). This event could explain the fractures in the oil zone that are filled with fine sediments, appear to cause displacement, and are lined by later recrystallization. However, there is no evidence for this stage of diagenesis in the lower reservoir regions, suggesting it did not occur in the oil-water contact and below. Placement of hydrocarbons in the reservoir rocks began to occur next (Cercone and Lohmann, 1987). Late rhombic dolomite cements with hydrocarbon inclusions is characteristic of the next stage of diagenesis, followed by milky calcite cement fillings with brine inclusions (Cercone and Lohmann, 1987). These cements entered the Niagaran and A-1 Carbonate formations as high temperature brines (>80°C), which are also responsible for forming geopetal sediment, pyrite, bitumen, dolomitic cements, and equant calcite spar (Wilson and Long, 1993). This would explain the recrystallization in the oil zone and could account for some of the fracture fill with pastel interference colors. The hydrocarbon inclusions in the dolomite cement would explain the pyrobitumen in the interior growth zones of every sample. If this speculation is true, many fractures in the oil zone and transition zone would be more recent due to the absence of cement in the void spaces. This would also explain why the cemented regions in the oil zone are affected by open fractures. However, micro fractures connecting to pores with secondary mineralization might be older depending on the age of these minerals. The origins of these features are still unclear and require further research.

As dolomitization occurred, the magnesium in the magnesium-rich water reacted with the calcite in the reef rock, causing replacement and recrystallization. The brines originated from Silurian seawater with concentrations between halite saturation and K-salt precipitation, but present day concentrations are too calcium rich to be attributed solely to dolomitization (Wilson and Long, 1993). The brine chemistry must have evolved from a dolomite stability field to a high Mg carbonate stability field in order to explain the secondary mineralization of the high Mg carbonates in the pore spaces of the samples. As the hypersaline brines entered the reefs, dolomitization, reaction with aluminosilicate minerals, removal of sulfate, and fluids from the A-1 potash salts all contributed to the calcium enrichment (Wilson and Long, 1993). During the diagenesis of the A-1 potash salts, concentrated Mg-K-Cl solutions were liberated and reacted with the dolomite, increasing the Ca concentration of the brine and the Mg concentration of the dolomite (Wilson and Long, 1993). Increased concentrations of Mg during dolomitization and evolution of the brine chemistry could have caused the precipitation of the high magnesium carbonate mineral in the pore spaces. Other

sources of increased magnesium concentrations can be attributed to skeletal calcium carbonate in warm seas, a higher calcite to aragonite ratio, and blue-green algae extracting Mg from sea water (Chilingar et al., 1967).

Potassium feldspar, fluorite, and quartz were all identified as accessory minerals in the oil zone and in the oil-water interface, and fluorite was identified in pores in the transitional region. In the oil zone, potassium feldspar and fluorite were imbedded in the matrix dolomite and contained interstitial dolomite inclusions. In the oil-water interface, fluorite, quartz, and phyllosilicate were imbedded in the matrix dolomite. The origins of these minerals are not known, but their placements in the matrix indicate that they are of the same generation as the matrix and could be authigenic. Authigenic feldspar has been identified in the southern belt, originating from depleted potassium levels in the brine, and in Ordovician carbonates in the basin (Wilson and Long, 1993). Authigenic quartz has also been observed in the Salina group (Wilson and Long, 1993), so it's possible these minerals precipitated in this reservoir. Also, authigenic minerals such as fluorite, celestite, zeolites, goethite, barite, clay minerals, phosphate, pyrolusite, gypsum, feldspar, micas, sphene, rutile, glauconite-chlorite, tourmaline, and pyrite-maracasite have been reported as able to form on the surface or within carbonates (Chilingar et al., 1967). If this is true, it could help explain these inclusions, the sequence of mineralization, and the pore fillings from the oil zone through the transitional region. More research is required to understand if these phases are authigenic or detrital, there origins, and how they relate to fluid evolution. The complex matrices in the oil zone and oil-water interface could be attributed to different reef organisms, fluid exposures, and detrital deposits than lower in the reservoir.

Systematic Relationships within the Reservoir

The sharp, euhedral pore shapes are abundant in all of the reservoir rocks. Along fractures and large pore boundaries in the sample matrices, anhedral grain boundaries are common. This is possibly due to fossil shapes and dissolution. Pores that are connected to fracture systems are commonly euhedral and filled with the high magnesium carbonate. Fractures walls and void spaces appeared to be composed of dolomite grains that were originally in the adjacent matrix as observed by the similar birefringence. However, there seems to be no relationship between fractures and pore sizes and distributions on the centimeter to millimeter scale. Lack of visible and open fractures in the oil-water contact increase the difficulty of observing these systematic relationships. There also does not seem to be a systematic relationship between locations in the reservoir and pore characteristics. All samples exhibited a broad range of pore sizes and distributions.

With increasing depth, pore spaces appeared to contain less organic content and more salts. Further research to quantify this relationship is needed for confirmation, but this could be caused by decreasing oil volume and increasing salinity or salt plugging with depth. Unique to the fracture fills in the transition region is the presence of dolomite fragments that appear to be stained or affected by either epoxy or another fluid. If this is not caused by epoxy, it could be due to thin films of brine left on the minerals or dissolution of minerals during CO_2 flow (DePaolo and Cole, 2013). The presence of some organic material in the transitional region and below the transitional region indicate that the oil-water interface may have migrated over time.

Effects of CO_2 Flooding

Immiscibility between injected CO_2 and reservoir fluids indicates that the CO_2 will not displace all of the original fluids, which is the case with water and oil (Benson and Cole, 2008). To some extent the CO_2 dissolves in the brine and mobilizes it, but leaves behind residual CO_2 in the pores and thin films of brine (DePaolo and Cole, 2013). Some of the water and oil would be trapped in the pores due to bypassing CO_2, and the amount of pore space occupied by CO_2 is controlled by the multiphase flow relationship (Benson and Cole, 2008). This limits the pore volume that CO_2 can occupy, but CO_2 of residual saturation remains trapped in the pores by water capillary pressures (Benson and Cole, 2008). Residual oil can be seen in the pore spaces throughout the reservoir as brown, spherical features.

To mobilize the brine during injection, high pressures are required to overcome capillary pressures (DePaolo and Cole, 2013). Reservoir pressures are affected over a larger volume than the volume that experiences flooding, but returns to equilibrium after injection (DePaolo and Cole, 2013). If these initial pressures are too high, fractures can form. It is possible that the open fractures in the oil zone and in the transitional region were caused by injection. These fractures must have occurred after cement fill, and CO_2 flooding explains the organic content. Dissolved CO_2 acidifies the fluids and causes dissolution of carbonate cements and feldspars and, over time, secondary mineralization of carbonate minerals and clays (Benson and Cole, 2008). In the short term this could decrease porosity and permeability, decrease the integrity of the reservoir rock, and modify fluid migration, but porosity and permeability would increase over a long period of time as minerals precipitate. Dissolution and brine films explain the dolomite grains in the transitional region that appear to be altered. It also explains why some pore edges and fracture linings are anhedral.

CONCLUSIONS

These reefs exhibit complex depositional and diagenesis patterns that created lateral and vertical heterogeneity in rock properties today. The variations in mineralogy throughout the reservoir can be attributed to differences in depositional environments and diagenesis. Samples containing siliceous minerals may have come in contact with off reef material and detrital deposits. Variation in diagenesis caused heterogeneity in pore characteristics, cement infillings, and fractures. The oil zone likely experienced shear fracturing and subsequent cement fill, but these features are not observed lower in the reservoir. Porosity does not vary obviously with depth, but more organic content and fewer salts were observed higher in the oil zone and in the oil-water contact. This may be due to exposure to brines over time. Correlation to ancient reefs and diagenesis included the destruction of reef fabrics from recrystallization, the inability for XRD to detect minor mineralogies, and small sample size.

Modern day CO_2 flooding may have caused fracturing with high pressure injections, altering mineral and pore boundaries by dissolution, or formation of new precipitates. Ultimately, this would affect fluid pathways, porosity, and permeability. Monitoring the well and reservoir rocks would mitigate any potential problems relating to CO_2 injection and increase the understanding of the long term fate of CO_2. Over time, more rock property analyses should be conducted to study migration pathways, dissolution, mineralization, and how porosity and permeability are affected.

RECOMMENDATIONS FOR FUTURE WORK

Future work could include further petrophysical characterization to examine porosity and permeability of the samples. For example, Mercury Injection Capillary Pressure (MICP) analysis of the intact core samples may help quantify these parameters. More detailed image analysis with Avizo, Fiji, and Ilastik may also provide more information about porosity, including determining both vertical and horizontal permeability for specific zones in the XCT and micro XCT scans. If one can determine the origin of fractures and the generation of minerals along the fractures, it would provide insight about whether CO_2 injection overpressurized these rocks, and whether the injection induced dissolution and mineralization. The degree of salt plugging should also be quantified to give better understanding of reservoir pressure, available pore space, and how this varies with depth.

Thin and thick sections should be made for continued analysis of intact core from depths 5606', 5690', and 5700' using similar techniques. Carbon isotope analysis of vug filling materials can be used to determine whether carbonate vug infillings, such as those observed from the 5690' intact core, are isotopically heavier than the surrounding matrix. If it is, it could be indicative that the high magnesium carbonate mineral is forming because of CO_2. More chemical analysis of the thin sections can provide more insight to variations in the matrix across the slides. These analyses can also be compared to other samples in the two Michigan reef trends to better understand variations in different reef positions. Incorporating well logs may help understand changes in density and porosity in the samples and indicate presence of organic content. Monitoring pH levels and gathering data on how carbonates are affected by acidic environments would aid in mitigating deterioration. These analyses should be continued during and after carbon dioxide injection to better understand long term effects on mineralogy, porosity, and permeability.

.

REFERENCES CITED

Benson, S. M. and Cole, D. R., 2008, CO_2 sequestration in deep sedimentary formations. Elements 4 (5), In: Carbon Dioxide Sequestration, D. R. Cole and E. H. Oelkers (eds.), p. 305-310.

Carbon sequestration atlas of the United States and Canada, 2015, Albany, OR, National Energy Technology Laboratory.

Caughlin, W.G., Lucia, F.J., and Mciver, N.L., 1976, The Detection and Development of Silurian Reefs in Northern Michigan: Geophysics, v. 41, p. 646–658, doi: 10.1190/1.1440640.

Cercone, K.R., and Lohmann, C.K., 1987, Late Burial Diagenesis of Niagaran (Middle Silurian) Pinnacle Reefs in Michigan Basin: AAPG Bulletin, v. 71, doi: 10.1306/94886d62-1704-11d7-8645000102c1865d.

Chilingar, G.V., Bissell, H.J., and Fairbridge, R.W., 1967, Carbonate rocks: physical and chemical aspects: Amsterdam, Elsevier.

DePaolo, D. J and Cole, D. R., 2013, Geochemistry of geologic carbon sequestration. An overview. Rev Mineral. Geochem. 77, p. 1-14.

Dooley, J.J., Dahowski, R.T., Davidson, C.L., Wise, M.A., Gupta, N., Kim, S.H., and Malone, E.L., 2006, Carbon dioxide capture geologic storage: a core element of a global energy technology strategy to address climate change: College Park, MD, Battelle, Joint Global Change Research Institute.

Friedman, G.M., and Kopaska-Merkel, D.C., 1991, Late Silurian pinnacle reefs of the Michigan Basin: Geological Society of America Special Papers Early Sedimentary Evolution of the Michigan Basin, p. 89–100, doi: 10.1130/spe256-p89.

Gardner, W.C., and, Bray, E.E., 1984, Oils and source rocks of Niagaran reefs (Silurian) in the Michigan basin: AAPG Studies in Geology, v. 18, p. 33–44.

Gill, D., 1979, Differential Entrapment of Oil and Gas in Niagaran Pinnacle-Reef Belt of Northern Michigan: AAPG Bulletin, v. 63, doi: 10.1306/2f91819e-16ce-11d7-8645000102c1865d.

Grammer, M., Noack, A., Qualman, H., Ritter-Varga, A., Wold, J., Sandomierski, A., and Harisson, W.B., 2010, Integrated Reservoir Characterization of Silurian (Niagaran) "Pinnacle" Reefs in the Michigan Basin– New Insights Into a Mature Reef Play: Datapages, Inc., http://www.searchanddiscovery.com/abstracts/html/2017/90291ace/abstracts/2609902.html (accessed April 2018).

Huh, J.M., Briggs, L.I., and Gill, D., 1977, Depositional environments of pinnacle reefs, Niagara and Salina Groups, northern shelf, Michigan basin: AAPG Studies in Geology, v. 5, p. 1–20.

Modroo, A., Goodman, W., Paul, D., and Padilla, A., 2014, Seismic-based porosity prediction in the Silurian Niagaran Formation reefs of Northern Michigan: An integrated case study: SEG Technical Program Expanded Abstracts 2014, doi: 10.1190/segam2014-0779.1.

Oelkers, E.H., Gislason, S.R., and Matter, J., 2008, Mineral Carbonation of CO2: Elements, v. 4, p. 333–337, doi: 10.2113/gselements.4.5.333.

Rine, M., Caruthers, A.H., Kaczmarek, S., and Harrison, W.B., 2017, A New Facies Architecture Model for the Silurian Niagaran Pinnacle Reef Complexes of the Michigan Basin: SEPM Special Publications, v. 109, doi: 10.2110/sepmsp.109.02.

Schaetzl, R.J. Hydrocarbons: Oil and Gas: Geography of Michigan and the Great Lakes Region, http://geo.msu.edu/extra/geogmich/oil&gas.html (accessed April 2018).

Sears, S.O., and Lucia, F.J., 1979, Reef-growth model for Silurian pinnacle reefs, northern Michigan reef trend: Geology, v. 7, p. 299, doi: 10.1130/0091-7613(1979)7<299:rmfspr>2.0.co;2.

Sonnenfeld, P., and Al-Aasm, I., 1991, The Salina evaporites in the Michigan Basin: Geological Society of America Special Papers Early Sedimentary Evolution of the Michigan Basin, p. 139–154, doi: 10.1130/spe256-p139.

Wilson, T.P., and Long, D.T., 1993, Geochemistry and isotope chemistry of CaNaCl brines in Silurian strata, Michigan Basin, U.S.A.: Applied Geochemistry, v. 8, p. 507–524, doi: 10.1016/0883-2927(93)90079-v.

APPENDIX

Sample Acquisition Data and Reservoir Position

Sample	Depth	Location in the Reservoir
Trim 30	5588’	Above oil-water contact
Intact Core 5606.1’	5606.1’	Above oil-water contact
Trim 25	5630’	Within oil-water contact
Trim 20	5655’	Transitional region from oil to water
Intact Core 5690.25’	5690.25’	Below oil-water contact
Intact Core 5700’	5700’	Below oil-water contact

Summary of Pore Characteristics

Depth (ft.)	Reservoir Location	Porosity	Pore Sizes	Pore Fillings	Pore Shapes
5588'	Above oil-water contact	Heterogeneous, Moderate and high	Most on the mm to µm scale	High Mg carb, salts, fluorite, barite-celesetite, organic material	Euhedral and anhedral
5630'	Within oil-water interface	Heterogeneous, Moderate and high	cm to µm scale	High Mg carb, halite, organic material	Euhedral and anhedral
5655'	Transitional region from oil to water	Heterogeneous, Moderate and high	Some on the cm scale, most on the mm to µm scale	Anh, high Mg carbonate, salts, fluorite, sulfide, organic material	Euhedral and anhedral
5690.25'	Below oil-water contact			Dol, anh, halite, calcium chloride, sulfide	Euhedral

Summary of Sample Mineralogies and Fracture Characteristics

Depth (ft.)	Reservoir Location	Fracture types	Filling Minerals	Aperture Size
5588'	Above oil-water contact	One large system, stylolite fractures	Dolomite, organic material., fine sediments	Up to .3 mm
5630'	Within oil-water interface	One small system	Dolomite, cc, organic material	Discontinuous, µm scale
5655'	Transitional region from oil to water	One large system	Dolo	Up to 1 mm
5690.25'	Below oil-water contact	At least one fracture system connecting to a vug		